RESEARCH PAPER

Low-Velocity Impact Damage Quantification on Sandwich Panels by Thermographic and Ultrasonic Procedures

A. Pirinu[1] · A. Saponaro[1] · R. Nobile[1] · F. W. Panella[1]

Abstract

Composite sandwich structures are widely used for their mechanical properties combined to lightweight. However, damage area quantification caused by low velocity impacts represents generally a crucial task in sandwich composites. In the last years, recent advantages of thermographic devices offer new promising and different real-time industrial and engineering applications where lower computation time, accuracy of results and convenient cost are required. The present research deals with the comparison of standard or latest image-processing methods proposed for pulsed thermography regarding their suitability for determining the impact damage area in sandwich materials made of Aluminium core an a GFRP laminated skins. The Infra-Red processed results are compared with the advanced ultrasonic Phased array method commonly employed in the industrial Non-Destructive Testing. Specifically, the damage area quantification is performed by means of an appropriate MATLAB binarization algorithm for the post-processing of acquired thermal and ultrasonic maps. The data results verify the effectiveness of the image-processing thermographic technique combined to advanced processing approaches for the quantitative assessment of impact damage in sandwich component.

Keywords Aluminium foam · GFRP · Impact sizing · Sandwich panels · Thermography · Ultrasonic technique

State of the Art

Nowadays, composite sandwich structures are widely employed in the aerospace, marine and civil applications for their physical and mechanical properties, such as sound insulation, high strength and stiffness, lightweight, and corrosion resistance properties [1–3]. The sandwich structures are composed by two face-sheets of stiff and strong materials (such as steel, aluminium alloys, or fibre reinforced polymers) and a lightweight core material with a low modulus (such as metallic or polymeric foams, wood or honeycomb structures) [2, 4]. Recently, the Aluminium Foam Sandwich is increasingly employed for lightweight structures in high-speed marine and terrestrial vehicles applications because they provide high passenger comfort with low weight and high-damping capacity [5–7]. In particular, the ship construction requires the high processing flexibility due to the limited series of ships' production [6, 8].

However, the susceptibility to impact damage represents one of the most critical drawbacks that could occur in sandwich elements [9–11]. In fact, during the production phase, maintenance cycle or service life, sandwich structures could be subjected to a range of external shocks, especially Low-Velocity Impacts (LVI), such as the falling of tools, bird strikes or in-flight hail [1, 12–14]. In addition, these LVI damages may be not visible as a confluence of laminate translucent or specific multi-layer configuration [15–17]. Clearly, the presence of various LVI damages could severely degrade the mechanical behaviour of AFS components, which are satisfy required to an acceptable level of structural integrity in accordance with Damage Tolerance requirements [18]. Therefore, the Non-Destructive Techniques (NDT) are required for the damage identification and reliable quantification of defects from impacts, avoiding excessive maintenance and repair cycles [19]. There are many ND techniques employed for the LVI damages in sandwich structures, such as radiography, shearography, Ultrasonic Testing (UT), Visual Inspection (VI), Vibration Analysis (VA), Acoustic Emission (AE) or Infrared Thermography (IRT), whose their continuous development is still on-going in terms of new inspection procedures and

✉ F. W. Panella
  francesco.panella@unisalento.it

1   Department of Engineering for Innovation, University
    of Salento, Via Per Monteroni, 73100 Lecce, LE, Italy

advanced processing approaches [19–22]. However, the main in-service demands on NDT methods consist of simplicity, rapid application and reliability, even if each method includes different advantages or limitations [19, 20].

For example, the Ultrasonic Phased Array (UPA) testing is a promising method for defect detection and damage size quantification on internal structure on inspected component [23, 24]. Thus, UPA systems remain excellent tools for ND inspections during manufacturing process or maintenance phase to ensure high-quality of composite structures [19, 23, 25]. However, the limitations of UPA technology includes the difficulty of set up and the level of skills required for operators to ensure accurate testing [19]. In addition, Pulsed Thermography (PT) is also considered a valid technique that could provide useful information for the material characterization through the visualization of the thermal signal impact damage [19, 26]. Specifically, while analysing the initiation and propagation of impact damage, the PT analysis could circumscribe the whole area affected by the impact damage and could identify the bands of increasing damage [19]. In addition, the technological progress provides new IR devices more sophisticated, lighter and low-cost for new applications, which requires a continuous improvement of data analysis methods [19].

Numerous research studies have been conducted to highlight advantages and limitations of the Pulsed Thermographic in the detection and quantification of impact damage for composite materials [16, 27–29]. However, really few works [16, 26, 27] are conducted to compare the main processing approaches for PT methods not only for the defect detection (internal structure or fibre breakage), but also for the sizing quantification of impact damage areas on sandwich structure. The present work is focused on the size characterization of Low-Velocity Impact damage on laminated AFS sandwich elements by processing thermal measurements and ultrasonic data. Two Non-Destructive methods are employed: Pulsed Thermography and Ultrasonic Phased Array.

Both processed thermal maps and the ultrasonic C-Scan maps were post-processed with customized routines developed in MATLAB environment for the binarization of the raw data and the subsequent quantification of the damaged areas. A high variability is observed in AFS series in terms of impact damage sizing and shape due to stochastic internal morphology and non-uniform local foam density. The final results demonstrated the effective potentiality of this combined ND inspection strategy for a proper quantification of impact damage in sandwich panels.

Materials and Methods

Sandwich Materials

Aluminium foam/ GFRP sandwich

The AFS components that have been considered in this study have a core in AlSi 10 Mg closed cell aluminium foam manufactured by Alulight as shown in Fig. 1 (a). Specifically, two plates of different thicknesses ($620 \times 620 \times 20$ mm and $620 \times 620 \times 30$ mm) have been used. The skins consist of a simple and thin stacking sequence [0°/90°/+45°/-45°] and have been laminated directly on the flat surfaces of the aluminium foam plates using a hand lay-up process and vacuum bag to avoid porosity and to remove the resin excess, as shown in Fig. 1 (b).

Concerning the skin constituent, the selected matrix is a two-component low viscosity epoxy resin ELANTAS EC-147 with hardener W-147, generally employed for nautical applications. As reported in Table 1, two glass fiber E-type fabrics are selected for AFS batches, precisely the PLAIN fabric with a density of 100 g/m^2 for AFS-20 series

(a)   (b)
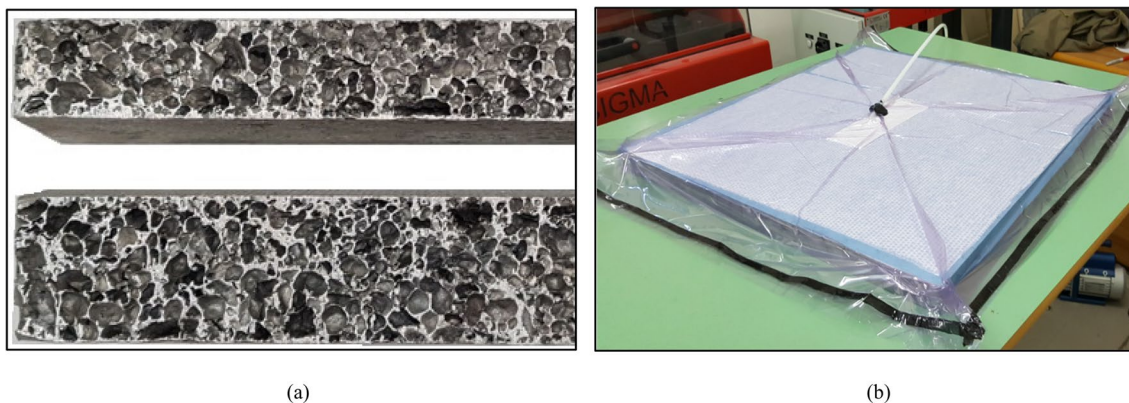
Fig. 1 (a) Sections of Alulight panels of 20 mm and 30 mm in thickness; (b) vacuum bag after hand lay-up lamination process of AFS sandwich panels

Table 1 Physical proprieties of constituent materials for two sandwich batches

ID AFS type	N.° of impacted AFS samples	Dim [mm^3]	Average Foam thickness [mm]	Core aluminium material	Average Density of AFS samples [kg/m^3]	Epoxy Resin of GFRP face-sheets	Glass fabric of GFRP face-sheets	Glass fabric density [g/m^2]	Layout of GFRP face-sheets
AFS-20 samples	8	200×110 ×20	20	AlSi10Mg base alloy	408.5	ELANTAS EC 147 / W 147	Plain	100	[0° / 90°/ +45°/ -45°]
AFS-30 samples	15	200×110 ×30	30		437.03	ELANTAS EC 147 / W 147	Twill	160	[0° / 90°/ +45°/ -45°]

and the TWILL fabric with a density of 160 g/m^2 for AFS-30 series. The use of different fabrics, plain for 20 mm and twill for 30 mm thick foam, allow to obtain a comparable stiffness ratio between skin and foam independently by foam thickness. However, this choice affects the impact damage, therefore the comparisons of the UT and IRT results were conducted separately on the AFS-20 and AFS-30 samples,

These different GFRP fabrics are employed to build a suitable configuration for the AFS elements in terms of lowest weight of the samples taking into account the thickness of the core. In addition, this interface could offer an improved performance in terms of adhesion and mechanical properties with a slight variation of weight/area ratio on the final element [28]. The skins have showed to provide a uniform mechanical behaviour in terms of stiffness and resistance to crack propagation [30, 31]. The laminated sandwich panels were subsequently cut to obtain two batches of specimens for impact tests, indicated as AFS-20 and AFS-30 based on their specific core thickness.

The foam density has been evaluated for each AFS sample, using a balance PCE-LSI 620. This balance provides a high measuring accuracy, with a weighing range of up to 620 g and a resolution of 0.001 g. Final, the foam core density value is calculated as

$$\rho_{foam} = \frac{m_{AFS}}{V_C} \tag{1}$$

where the m_{AFS} term represents the measured mass [kg] of the specific AFS sample and V_C [m^3] variable indicates the calculated volume of AFS element, whose theoretical dimensions [in mm^3] are reported in Table 1 for both AFS batches.

Impact tests

The Low-Velocity Impact tests are conducted on a Fractovis Plus drop test machine according to ASTM 7136 standard (Fig. 2). Figure 3 (a) illustrates the clamping system of drop test machine avoids the lateral slipping of AFS specimens that are fixed on the base with a rigid metallic circular plate (of diameter of 40 mm) without crushing effects, as reported in Fig. 3 (b).

Fig. 2 Drop-weight impact test machine used for AFS elements

(a)   (b)
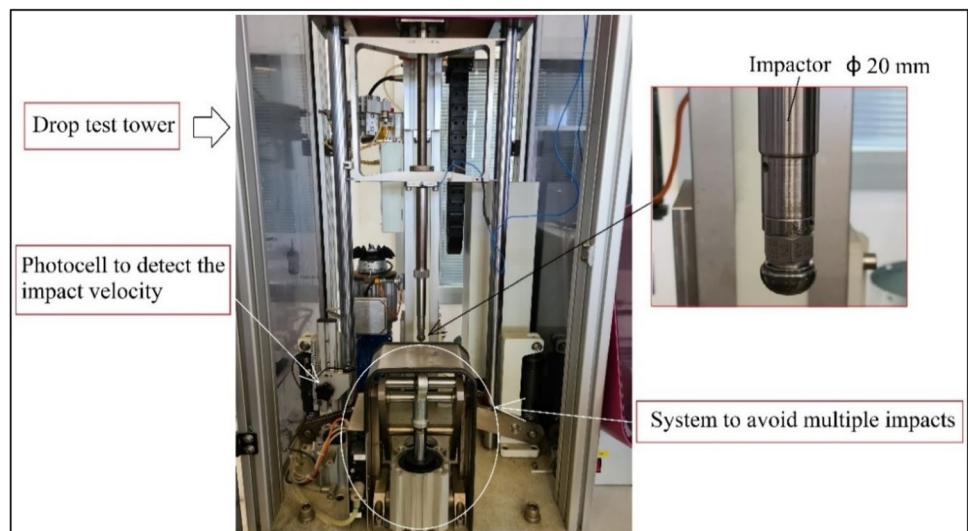
Fig. 3 (a) Clamping system and (b) AFS sample fixed with a rigid metallic circular plate (diameter equal to 40 mm)

Specifically, a central impact was performed on each specimen to avoid detachment of the skins near the external edges and for better inspection convenience by means IRT and UT methods. The impactor consists of a hemispherical tip with a diameter of 20 mm with an impacting mass of approximately 5.045 kg.

In the Table 2, the experimental parameters used for impact tests of the two AFS batches are reported. As indicated, specific combinations of impact velocity and impact energy was selected for the two different sandwich series that exhibit different failure modes and an interesting impact area variability, based on previous experiences [30].

As representative examples, Fig. 4 show two impact damages on AFS 30 and AFS 20 specimens, where the skin cracking and a partial detachment are observed in both elements.

Thermographic Inspection

In the present work, the pulsed thermography in reflection mode was employed for preliminary inspections on laminated sandwich panels and on the various AFS specimens obtained from the latter. Specifically, the PT technique is a suitable NDT procedure for a quick inspection of large surface industrial elements.

For each IR inspection, after impact tests, all surfaces examined were treated with the same high temperature matte black paint with an emissivity of 0.93 to reduce thermal reflections and non-uniform heating effects. The micro-bolometric thermal camera FLIR A655sc was employed for both thermographic setups (Fig. 5). This thermal camera is equipped with an uncooled micro-bolometric sensor, that provides thermal images at 640×480 pixels of high quality and measurement accuracy with temperature differences of 30 mK.

Based on previous ND experiences [30, 32–34], an IR camera – object distance of 1600 mm is selected for AFS laminated panels, whilst a distance of 1100 mm is employed for sandwich specimens. Both thermographic setups consist of an optical thermal source (halogen lamps) and a signal generator to provide a thermal pulse as single square wave-form. For the experiments, four halogen lamps of 1000 W were used for each AFS laminate panel, while only two halogen lamps were used for each AFS specimen (Fig. 6).

For different inspections, the thermographic parameters were selected for AFS elements based on previous experience [30], as reported in Table 3, where three different heating times of 3 s, 5 s and 8 s were employed for each inspection on AFS elements. As shown in Fig. 5 (b), in the thermal map reported as an example, obtained after 0.32 s from the end of the heating of 3 s, the performed inspections seem

Table 2 Experimental parameters used for impact tests on AFS batches

Series	Specimen	Impact Energy [J]	Impact Velocity [m/s]	Impact Height [mm]	Total mass of Impactor [Kg]
AFS -20	P4, P5, P6, P11, P13, P15, P17, P19	2.5	1	51	5.045
AFS—30	P4, P5, P6, P8, P10, P15, P16, P19, P21, P23, P24, P27, P28, P31, P33	10	2	202	5.045
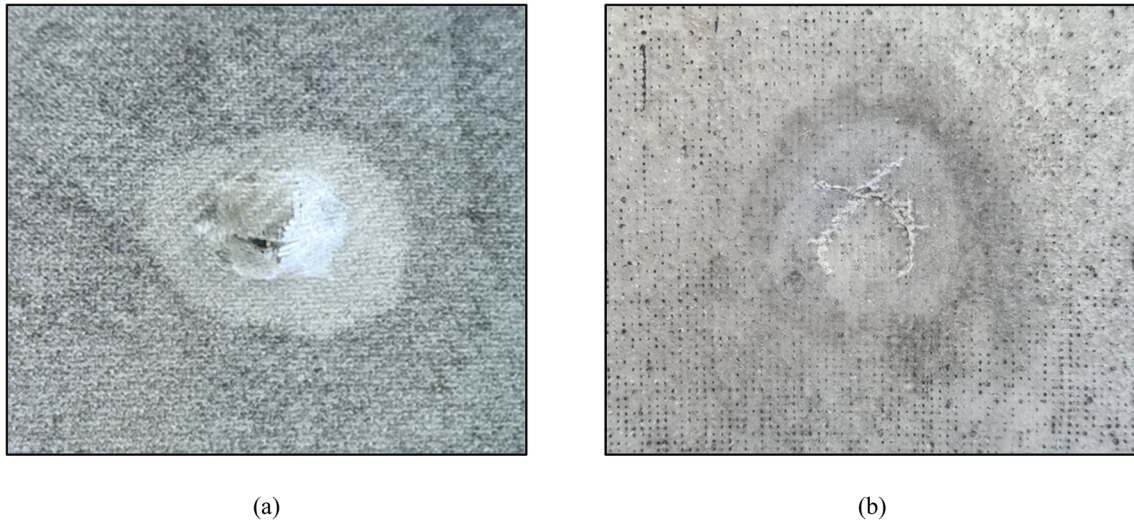
Fig. 4 (a) Example of AFS 30 sample and (b) AFS 20 specimen after the impact at v = 2 m/s and v = 1 m/s, respectively
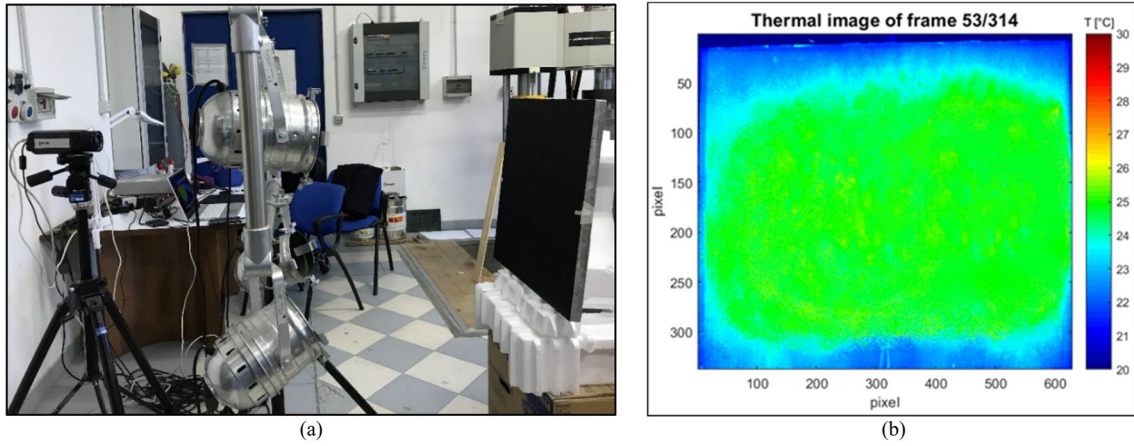
Fig. 5 (a) Pulsed thermographic setup for inspection of the entire laminated AFS panels and (b) thermal map after 0.32 s after heating time of 3 s on the AFS-30 panel

Fig. 6 Experimental pulsed thermographic setup for inspection of AFS elements

Table 3 Experimental parameters for IRT investigations

| Sandwich series	Defect depth	Frame rate [Hz]	Heating time [s]	Acquisition time [s]	Total frames
AFS-20 panels	0÷4	6.25	3	50	314
			5	100	625
			8	100	1000
AFS-30 panels			3	50	314
			5	100	625
			8	100	1000
AFS-20 samples			3	50	314
			5	100	625
			8	100	1000
AFS-30 samples			3	50	314
			5	100	625
			8	100	1000

to reveal no defects on the laminated skins for the AFS-30 panel.

Ultrasonic Inspection

An Olympus Omni-Scan MX portable unit was employed to perform the Phased Array (PA) ultrasonic analysis on impact damage of AFS elements (Fig. 7 (a)). The UT detector system is equipped with a 64-element Olympus probe (2.25L64-A2) with frequency of 2.25 MHz that results proper for the UT inspection on composite materials [34, 35]. This probe is fixed on a plexiglass wedge and connected to a Mini-wheel absolute encoder with a resolution of twelve steps/mm to perform the C-scan maps acquiring data in a synchronized way with the one-way motion of probe. The measurement probe-encoder system is positioned on a thermoplastic polymeric PLA support and guided along a straight path by an aluminium profile (Fig. 7 (b)) [32]. The C-Scan maps are visualized through a two-dimensional view of displayed data related to the inspected surface of the component.

Thus, the UT data are monitored in a real-time mode along a specific coordinate direction on X–Y plane. The ultrasonic PA scans are performed in contact mode employing a water-based coupling gel on the laminated skins of AFS samples. A preliminary calibration of the UT detector is conducted to define the ultrasonic parameters for the inspections, such as the specific ultrasonic velocity of sandwich material. The ultrasonic velocity of the material is estimated equal to 2700 m/s and the linear scans at 0 degree are conducted employing a constant gain of 8 dB [30].

(a)   (b)
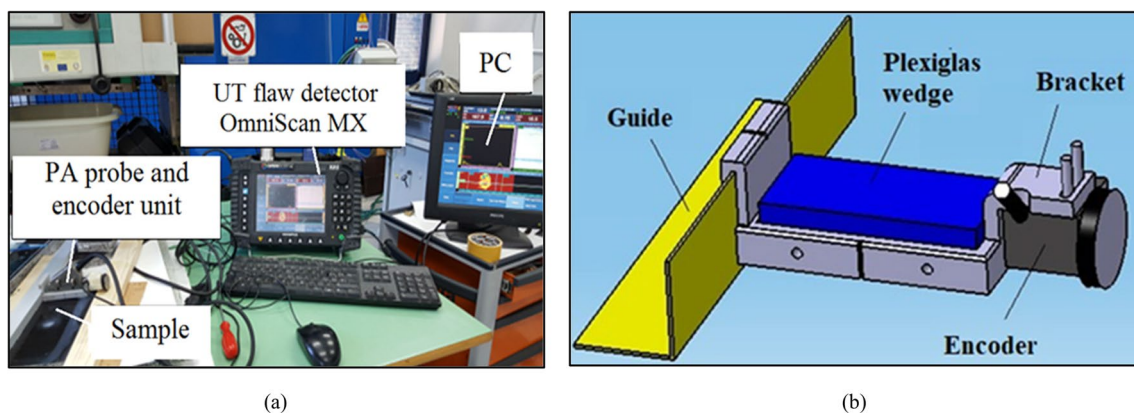
Fig. 7 (a) Experimental setup employed for ultrasonic Phased Array measurements and (b) Plexiglas wedge for probe UPA and encoder movement system, image from [29]

Processing Approaches

The present section describes the different processing approaches for PT technique and the binarization methods for the impact damage quantification through thermal and ultrasonic data.

Image Processing for PT

As described by different authors [36–38], advanced thermal signal processing methods have been proposed in the last twenties for the PT method in order to enhance the detection and quantification of material damages through signal-to-noise ratio or probability of detection improvements in industrial components [39–41].

Specifically, acquired thermal images are processed in time domain, frequency domain or different strategies (such as in principal component analysis), involving a series of advanced mathematical operations performed to get useful information [28, 41, 42]. These data processing techniques have several advantages and limitations in terms of defect detectability, computation time, signal-to-noise ratio, etc., therefore an automatic quantitative extraction of information combined with adequate processing time and appropriate thermal models represents a demanding challenge in the processing of thermal images [32, 33, 36, 43].

Based on the literature [32, 36–38], different well-established and advanced elaboration approaches proposed for thermographic pulsed technique are selected for sizing quantification of impact damages on AFS elements. These processing procedures are classified as multiple-maps or single-map processing methods based.on the processed output of raw data. Specifically, the multiple-maps processing methods include the thermal signal reconstructed and the Principal Component Thermographic techniques, whilst the single-map approaches consist of two statistical methods (Skewness and Kurtosis) and LBC-II procedures [32, 33].

Multiple-maps processing methods

Reconstructive Techniques The processing procedures based on the reconstruction include the signal reconstruction or TSR, first and second derivative methods [32, 33]. Thermal signal reconstructed (TSR) technique provides significant sensitivity improvement, used especially in noise filtering and data reduction that increases the signal-to-noise (SNR) performance than the raw thermal maps [44–46]. The mathematical origin of TSR technique comes from the Fourier's one-dimensional heat-transfer equation on a semi-infinite surface previously subjected to thermal excitation (Dirac delta) [44, 45]. Basically, this thermal response equation

of step-heating surface could be described as temperature evolution [°C] of free-defect zones in logarithmic scale with a slope of $-1/2$ and a constant of Q/e. Specifically, thermal signal reconstruction approach processes the thermal evolution of a pixel using a polynomial of nth degree, fitting the polynomial to a logarithmic sequence performing with least squares [43, 44] as

$$ln\left[\Delta T_{surf}(t)\right] = a_0 + a_1 * ln(t) + a_2 * [ln(t)]^2 + \cdots + a_n * [ln(t)]^n \tag{2}$$

where the full sequence of thermal rise $\Delta T_{surf}(t)$ of each pixel is built by the series of $(n+1)$ polynomial regression coefficients $a_0, a_1, a_2, \ldots, a_n$ [44, 46]. The choice of small nth order provides satisfactory results in terms of reducing oscillations in the processed sequence and a fourth and fifth-order polynomial order effectively acts as a low pass filter to smooth the data without reconstructing the noise [29, 44, 46, 47].

However, a fifth or sixth order polynomial seems effectively to provide a low pass filter to smooth the data without reconstructing the noise [32, 48]. In addition, recently authors proposed the evaluation of coefficient images for rapid fully automated processing of the three best polynomial coefficient images in an RGB basis, to create a unique "composite" image of the defects to simplify the NDE operations during manufacturing or maintenance industrial processes [49, 50]. The $(n+1)$ images processing approach results more suitable in terms of data analysis and reduced computation time [29, 50]. Different TSR processing techniques include the classic TSR approach consisting in the selecting of best reconstructive or derivative images associated with different depth range for qualitatively defects detection, while the simpler TSR coefficient approach is based on calculation of $(n+1)$ logarithmic polynomial coefficients for every full thermal sequence [50].

Principal Component Thermography Principal Component Thermography (PCT) technique proposed by Rajic [32, 51, 52] is based on an eigenvector transform that applies an orthogonal transformation to acquired thermal data through singular value decomposition (SVD) method to achieve compact data statistical representation of contrasts variations, associated with defects presence [53]. Before applying decomposition, the selected 3D matrix of thermal image sequence is reshaped into 2D array, where the columns and rows contain the spatial and temporal information, respectively. Thus, original image sequence $(N_x \times N_y \times N_t)$ of N_x and N_y pixel dimensions and N_t number of frames is transformed in the matrix A $(M \times N_t)$ through a decomposition processing where $M = N_x \times N_y$. Then, matrix A is adjusted by subtracting the mean value along time dimension and by eigenvectors and eigenvalues decomposition. Any $M \times N$

matrix can be decomposed through SVD decomposition and calculated as [14, 52]:

$$A = U * D * V^T \tag{3}$$

where U is an M × N orthogonal matrix, D represents a diagonal N × N matrix containing singular values of A performing in the diagonal and VT is the transpose of N × N orthogonal time matrix whose columns represent the main components of the temporal variations [51]. Orthogonal statistical characteristics are contained in matrix U columns, known as empirical orthogonal functions (EOFs) describing spatial variations within the data [52]; similarly, in matrix VT rows the principal components (PCs) present characteristic time behaviour and associated to defect depth estimation [52]. The matrix U may be rearranged as a 3D matrix to produce EOF image sequence, given that first few EOFs describe largest variability in the thermal sequence and generally contain useful images. In fact, PCT numerical approach is an effective technique, but it was found that using the total time for sampling improves the PCT results and first seven EOF images gives better results.

Single-map processing methods

Statistical Methods The statistical processing methods are introduced for enhancing the automatic processing of an infrared sequence reducing human intervention [54]. In their works, Madruga et al. [54–56] proposes the higher-order statistics (HOS) analysis to achieve a rapid single-map image processing approach that provides a suitable compression of the most useful information into a unique image for each inspection.

In probability theory, the skewness is a common statistical method that include the third standardized central moment of the probability distribution. The skewness parameter represents a measure of symmetry, or more precisely, characterizing the lack of symmetry in a probability distribution of the temperature–time history, defined for each pixel as [54, 55]

$$Skewness = \frac{\sum_{k=1}^{N}(x_k - \mu)^3}{\sigma^3(N-1)} \tag{4}$$

where μ and σ are the mean and standard deviation respectively of random variable x.

The Kurtosis is the fourth standardized moment of the probability distribution that measures the relative flatness of the probability distribution related to the shape of a normal distribution in the temperature–time history on each pixel [54, 56]. Therefore, Kurtosis measurement reflects the degree to which the distribution is peaked, providing information of distribution height relative to the value of standard deviations, given as [55]

$$Kurtosis = \frac{\sum_{k=1}^{N}(x_k - \mu)^4}{\sigma^4(N-1)} \tag{5}$$

Therefore, these HOS parameters (third and fourth orders) are applied to TNDT showing to be a powerful tool for defect detection combined to high compression capabilities [54]. In this work, the third and the fourth HOS parameters are employed in the comparative analysis, because the skewness parameter results the most sensible parameter, but less dependent on the shallowest defects than kurtosis measurement, whose distribution shape results less affected by the deeper defect.

LBC-II Methods Finally, the LBC-II elaboration approach consists of a different contrast-based processing method proposed by the authors Panella and Pirinu in a previous work [32] that combines an enhancing defect inspection with a different contrast measurement where a local automated selection of defect-free reference zone is performed for each detect, providing a single contrast map elaborated [32, 33, 35]. The proposed approach provides processed contrast maps that maximize contrast values lying on defect border, leading to display local contrast variations, clearly recognizing flaw's borders for a proper damage sizing quantification [32, 33].

The LBC-II approach provides processed contrast map at a given time, applying a time filtration to compress the data information contained in the 3D thermal sequences into a single image, as observed for HOS methods [54, 55]. Specifically, for each [i, j]th pixel of a selected thermal image, this processing procedure computes automatically the absolute LBC-II contrast $C_{LBC-II(i,j)}^{std}$ [°C] calculated as [32]:

$$C_{LBC-II(i,j)}^{std} = \left| \Delta T_{LBC-II(i,j)}(t) \right| = \left| \sum_{t=t_{max}}^{t_{end}} \frac{\overline{N_{ROI(i,j)}(t)}}{(t_{end} - t_{max})} - \sum_{t=t_{max}}^{t_{end}} \frac{\overline{I_{ROI(i,j)}(t)}}{(t_{end} - t_{max})} \right| \tag{6}$$

where $(t_{end} - t_{max})$ represents the cooling phase of the thermal acquisition. The proposed contrast is computed between two ROIs, defined as average thermal data of an image subset $I_{ROI(i,j)}$ and the mean temperature of its neighbourhood area $N_{ROI(i,j)}$, in a similar automatization procedure proposed by another author [57, 58]. The $T_{I(i,j)}$ and $T_{N(i,j)}$ represents the temperature in a reference squared matrix zone (Dim. 3 × 3) and all around [i, j]th calculation point matrix zone (Dim. $p \times p$, with $p > 3$), respectively.

The specific apex 'std' is added for the proposed contrast parameter for a suitable distinction between three different contrast approaches of LBC-II evaluations [32]. In fact, two other computation approaches could be employed for image-processing elaboration, highlighting the contrast values of

undamaged (defined as $C^A_{LBC-II(i,j)}$) or of damaged (denoted as $C^B_{LBC-II(i,j)}$), evaluated such as [32]

$$C^A_{LBC-II(i,j)}(t) = +\Delta T_{LBC-II(i,j)}(t) \tag{7}$$

and

$$C^B_{LBC-II(i,j)}(t) = -\Delta T_{LBC-II(i,j)}(t) \tag{8}$$

Therefore, final elaborated contrast maps are processed highlighting the surrounding defect-free contrast values (defined as $C^A_{LBC-II(i,j)}(t)$) or defective contrast values (defined as $C^B_{LBC-II(i,j)}(t)$) [32].

Binarization Approaches

Binarization for thermal data

The quantitative analysis of impact damage seems to involve a defective depth of a couple of tenths of a mm (near the laminate-core interface), then short heating times (lower than 10 s) are employed for pulsed thermographic inspections, as reported in Table 3. In this case study, the quantification analysis for impact defect sizing as automated approach is performed [30, 40].

For a better characterization of the damage size, thermal maps were exported and manipulated in the MATLAB environment, where a processing routine is developed for

the binarization of different processing approaches, defining a threshold value of temperature selected based on the average values of defective and intact zones calculated in regions of interest (or ROIs). For impact sizing, a different thermal contrast definition is employed, the 'so-called' running contrast defined as:

$$\Delta T^{thr}_{run} = \frac{\overline{T_{def\_edge}} - \overline{T_i}}{\overline{T_i}} \tag{9}$$

where $\overline{T_{def\_edge}}$ and $\overline{T_i}$ represent the average temperatures in selected defective and defect-free ROIs of pixels in the single evaluated map. Preliminary analysis of different processed maps is performed to highlight the suitable average threshold running contrast value, employed for each processing quantification.

Specifically, the reference average value $\overline{T_{def\_edge}}$ is determined in customized five ROIs selected on near surroundings of impact area, where rapid variation of map parameters (thermal, statistical or LBC-II contrast values) is observed and clearly distinguished defective and un-damaged areas, as shown in example Fig. 8 (a) and in the relative iso-line trends reported in Fig. 8 (b).

Then, the estimated impact area on the different processed images is calculated as follows:

$$A_{IRT} = \left(\sum_{j=1}^{m} \sum_{i=1}^{n} P_{i,j} \right) * f_c \tag{10}$$

(a)   (b)
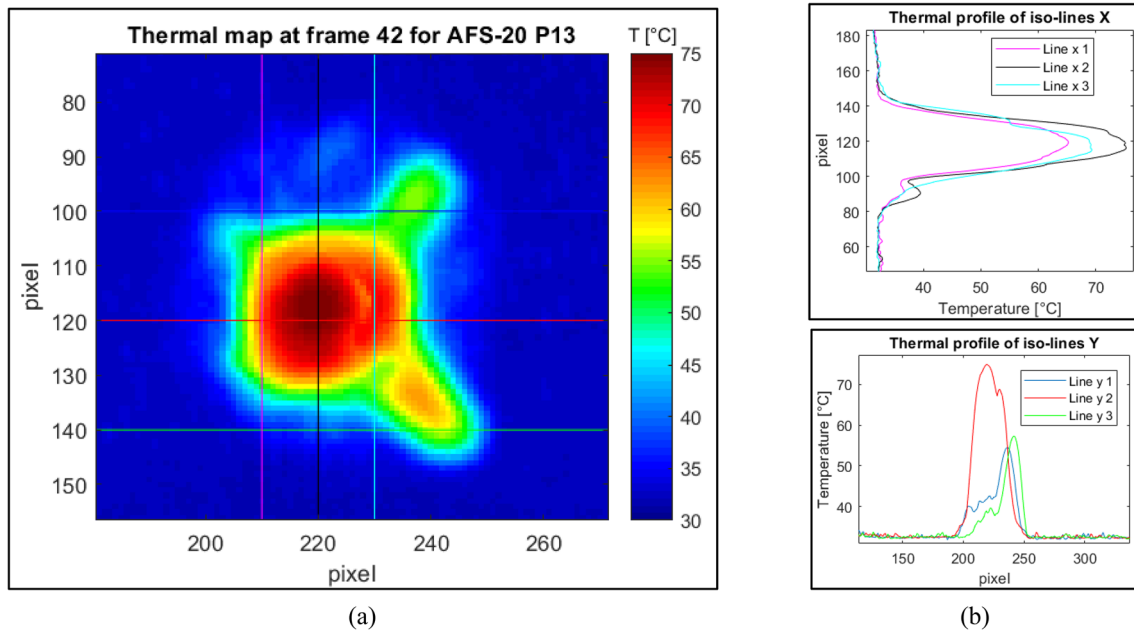
Fig. 8 (a) Thermal map with iso-lines along X and Y direction; (b) thermal profiles of iso-lines X (upper) and iso-lines Y (bottom) for AFS-20 P13 panel at 0.5 s from the end of heating

where $P_{i,j}$ represents the pixel having temperature that satisfies equation (11), in specific processed 2D image [Dim. m × n]; f_c the conversion factor employed in MATLAB code to convert pixels area in a mm² area, based on the well-known length sides of each panel. Since the length in pixels of the sides of the sample is known in the thermal images displayed, the areas in mm² relating to the impact damage were determined with a simple mathematical proportion, multiplying the value of the impact area (A_{IRT}) by the factor fc given by the ratio between area of the specimen in mm² and the same area in pixels of thermal image of thermal camera. Specifically, a selected [i, j]th pixel is included in the calculation (equation (10)) if its specific temperature satisfies the following relationship

$$T_{i,j} \geq \left(1 + \Delta T_{run}^{thr}\right) * T_{def\_edge} \qquad (11)$$

Therefore, the proposed binarization processing method consists of a simple procedure based on the threshold evaluation, that represent a suitable choice for a comparative analysis between different elaborated maps, where hot/ cold spot defective zones and different surrounding—defect edge contrast could occur.

Binarization for UT data

Concerning the ultrasonic measurements, the C-scan maps are exported using Tomo—View software and post-processed employing MATLAB codes. Specifically, a binarization analysis based on a threshold value is performed to determine the impact damage area of inspected sandwiches. The impact area is selected from this two-dimensional matrix of amplitudes map, not including the neighbouring areas of damage. The threshold amplitude values employed for the binarization processing of C-Scan map are determined considering the measured amplitude profile along three paths (the line 1, line 2 and line 3) on the UT map and determining the specific mean of the pixels' values that cross the boundaries of the damaged part, as shown in Fig. 9 (a).

This processing procedure was repeated for each of the three lines considered. The correct threshold value was then determined by making the arithmetic average of the three average values previously determined and equation expressed by the following:

$$A_{th} = \frac{\sum_{j=1}^{l} \left[\sum_{i=1}^{N} \frac{A_{ij}}{N} \right]}{l} \qquad (12)$$

where the index j indicates one of three lines of UT measurement, l indicates the total number of lines considered (l = 3), while the index i represents the specific pixel of the selected area and the term N is the number of total pixels considered on each line ($N = 8$); finally, the A_{ij} data represent the percentage amplitudes relative to each pixel considered in the impacted zone.

Results and Discussion

In the present section, a comparative analysis between UT and IRT results is performed for sizing evaluation of impact areas on AFS series. The impact area quantification through ultrasonic inspections represents the reference approach for PT processing methods.

UT Processing Results

In this paragraph, exported scan maps and binarization processing results for ultrasonic data are discussed (Figs. 11, 12, 13, 14, 15, 16, 17 and 18). Figures 10 (b), 13 (b), and 16 (b) show three examples of linear C-Scan (0°) scans with a local X–Y coordinate system on the two batches of AFS-20 and AFS-30 specimens. In addition, the Figs. 12, 15, and 18 show the binarized C-Scan maps related to three examples of data processing.

Concerning the AFS-20 P13 element, the specific geometry of the impact area presents an almost circular shape with two evident thin lateral wings observed in both binarized
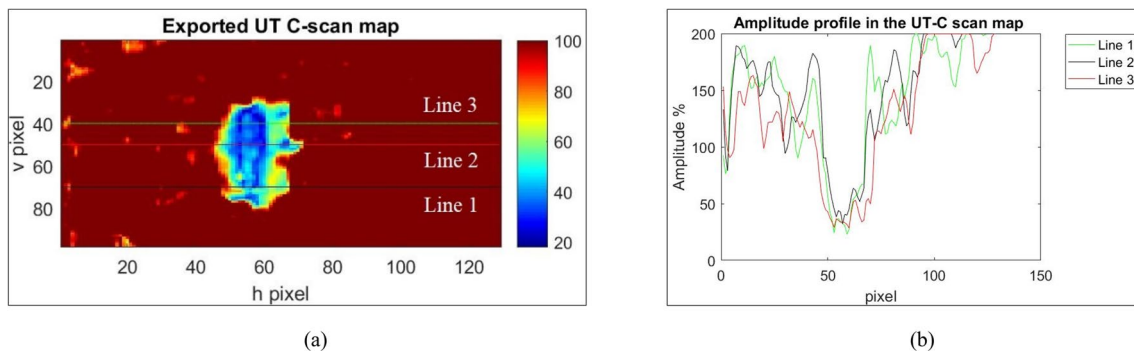

(a)   (b)

Fig. 9 (a) C-Scan map exported in MATLAB and (b) amplitude profiles used for the threshold level computation (A_{th}) for AFS-20 P18
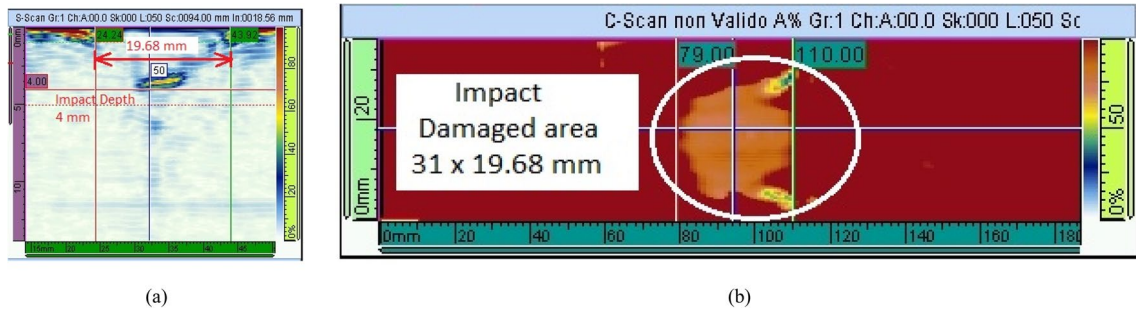
Fig. 10 (a) S-Scan (0°) and (b) C-Scan maps along the x axis for AFS-20 P13 sandwich element
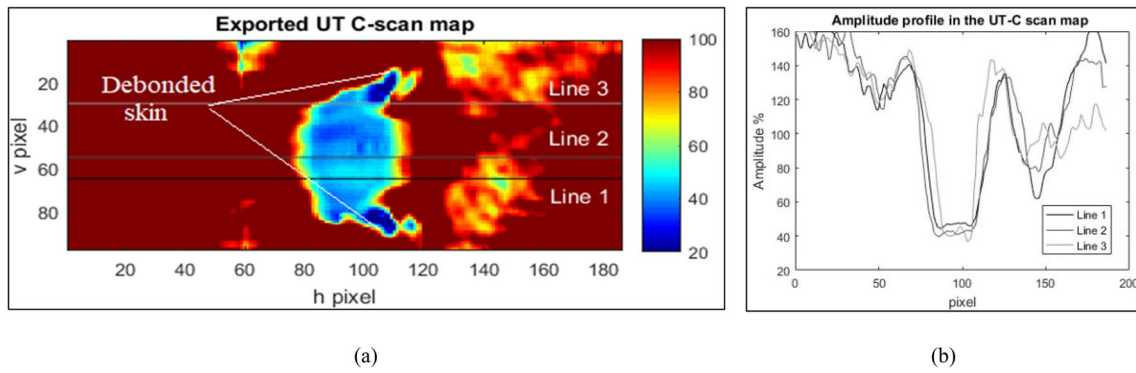

Fig. 11 (a) C-Scan map exported in Matlab and (b) amplitude profiles used for the threshold level computation (A_{th}) for AFS-20 P13

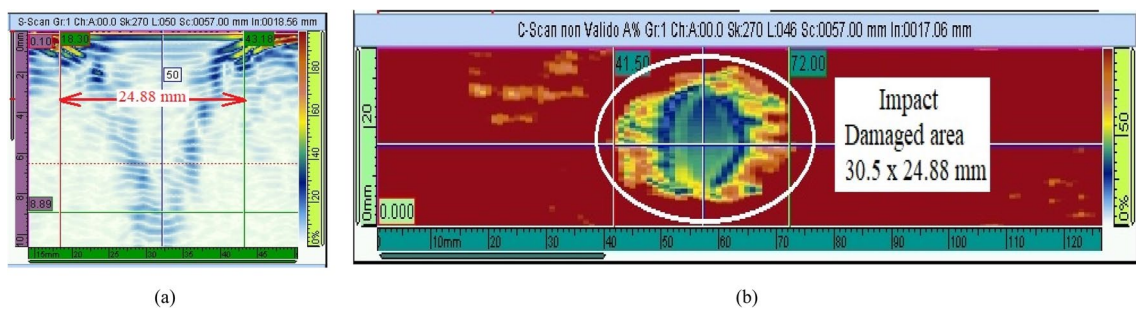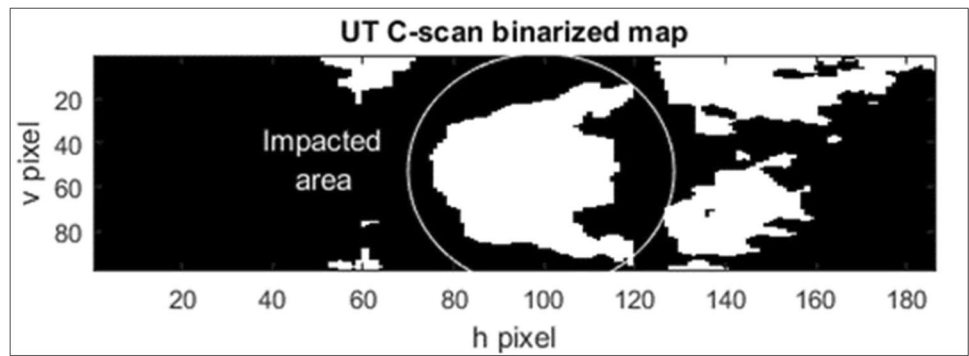**Fig. 12** Binarized C-Scan map of AFS-20 P13 sandwich element

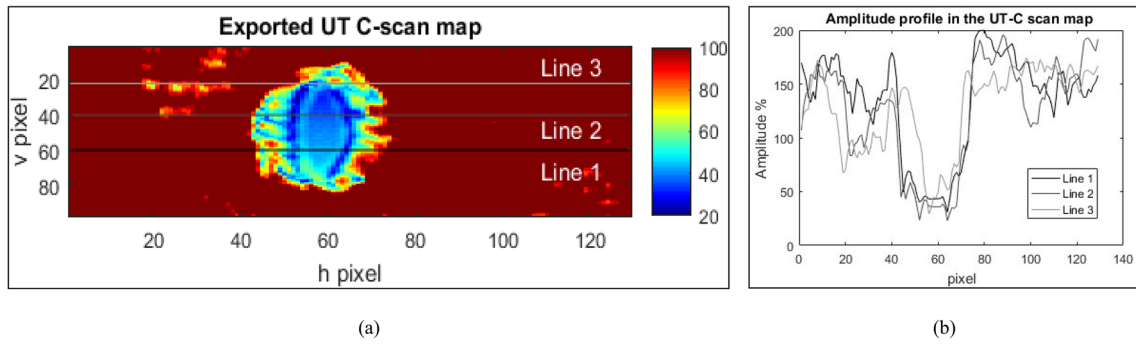**Fig. 13** (a) S-Scan map (0°) and (b) C-Scan map along the x axis for AFS-30 P21 element

Fig. 14 (a) C-Scan map exported in Matlab and (b) amplitude profiles used for the threshold level computation (A_{th}) for AFS-30 P21

Fig. 15 Binarized C-Scan map of AFS-30 P21 specimen
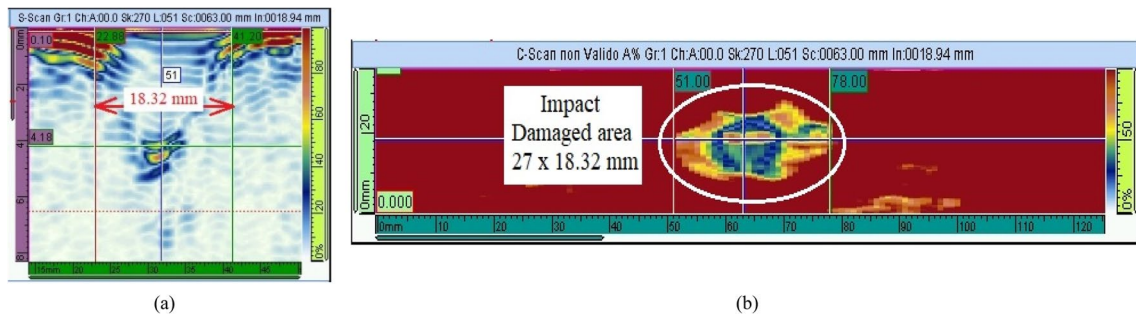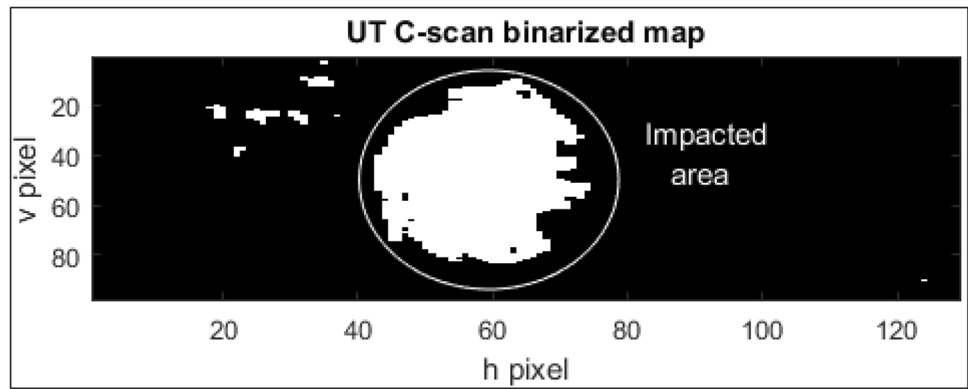

Fig. 16 (a) S-Scan at the 0° and (b) C-Scan maps along the x axis for AFS-30 P28 sample
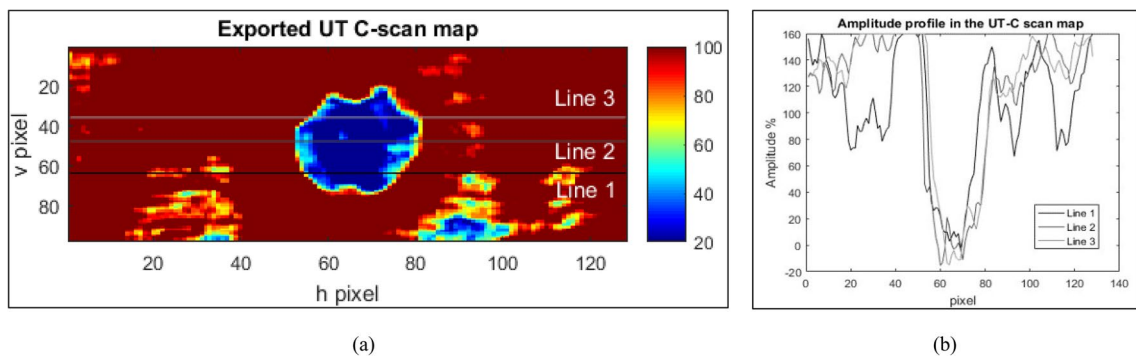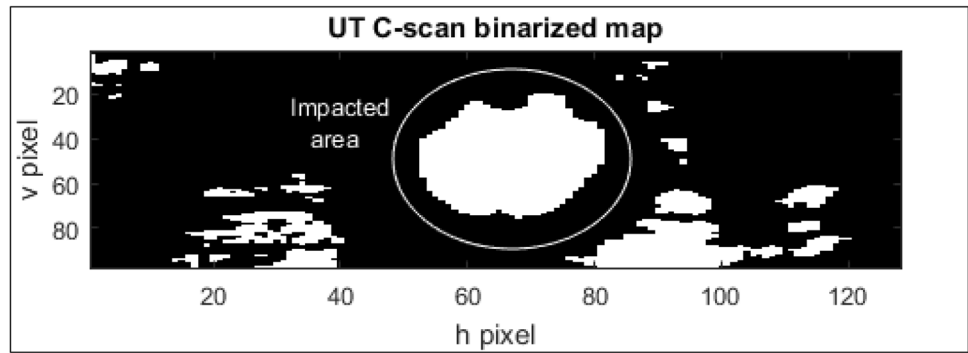

Fig. 17 (a) C-Scan map exported in Matlab and (b) amplitude profiles used for the threshold level computation (A_{th}) for AFS-30 P28

Fig. 18 Binarized C-Scan map of AFS-30 P28 specimen

UT C-scan binarized map

Table 4 UT quantification of impact damage on AFS-20 specimens

ID Sample	Estimated impact depth [mm]	Threshold amplitude A_{th} [%]	Damaged area on C-scan map [mm^2]	Impact area on binarized C-scan map A_{UT} [mm^2]	E [%]
AFS-20 P4	4.02	85.3	516.72	441.55	+17.0
AFS-20 P5	4.10	84.2	1319.70	961.46	+37.3
AFS-20 P6	4.05	63.4	500.00	334.30	+49.6
AFS-20 P11	4.08	65.3	443.02	320.53	+38.2
AFS-20 P13	4.12	93.9	610.08	869.50	- 29.8
AFS-20 P15	5.6	96.6	487.08	690.35	+29.4
AFS-20 P17	2.52	60.7	312.74	320.84	- 2.5
AFS-20 P19	3.72	83.6	490.05	359.64	+36.3

Table 5 Quantification of impact damage on the AFS-30 specimens

ID Sample	Estimated impact depth [mm]	Threshold amplitude A_{th} [%]	Damaged area on C-scan map [mm^2]	Impact area on binarized C-scan map A_{UT} [mm^2]	E [%]
AFS-30 P4	4.13	82.4	622.34	602.44	+3.30
AFS-30 P5	4.11	85.9	583.70	680.55	-14.23
AFS-30 P6	4.07	67.3	580.03	521.25	+11.28
AFS-30 P8	4.04	86.8	330.45	434.75	-23.99
AFS-30 P10	4.24	98.4	360.00	428.83	-16.05
AFS-30 P15	11.03	97.4	533.33	567.95	-6.10
AFS-30 P16	5.01	97.9	768.93	865.8	-11.19
AFS-30 P19	6.13	76.1	647.92	605.32	+7.04
AFS-30 P21	8.89	83.4	758.84	600.88	+26.29
AFS-30 P23	8.08	62.0	1061.61	901.32	+17.78
AFS-30 P24	6.87	67.3	946.56	812.15	+16.55
AFS-30 P27	4.59	85.9	894.04	1072.26	-16.62
AFS-30 P28	4.18	89.3	694.64	641.78	+8.24
AFS-30 P31	4.95	91.0	682.80	539.83	+26.48
AFS-30 P33	2.03	88.9	1337.77	1084.00	+23.41

IRT and UT maps, as shown in Figs. 12 and 15 (b), respectively. However, the threshold value employed for the binarization processing of UT map (Fig. 11 (a)-(b)) is estimated equal to 93.9% for the AFS-20 P13 element, as reported in the Table 4. For the specimens AFS-30 P21 and AFS-30 P28, the threshold values estimated with the binarization process of the UT map (Figs. 14 and 17) are equal to 83.4% and 89.3%, respectively.

For the impact area quantification, the measured pixel dimensions are estimated equal to 0.37×0.98 mm^2. Therefore, a conversion factor is employed for the impact damage sizing in the binarized ultrasonic maps.

Tables 4 and 5 report the results for the size quantification of impact damage for AFS-20 and AFS-30 samples, respectively. In addition, a percentage parameter E is also defined to assess the different size estimation between the damage area A_{C-Scan} evaluated on the C-Scan through the measurement cursors and the impact area A_{C-Scan_bin} evaluated through the binarization approach.

Specifically, this percentage parameter is computed by the following equation:

$$E[\%] = \frac{A_{C-Scan} - A_{C-Scan\_bin}}{A_{C-Scan\_bin}} * 100 \qquad (13)$$

In the Tables 4 and 5, the calculated values of percentage parameter E are summarized for the two AFS batches, where positive and negative data are observed.

The obtained depth and size data of impact damages are also correlated to the foam density values for both AFS series. The Fig. 19 (a) shows the impact depth data estimated through the S-scans performed at 0° as function of the foam density data for both AFS series. In this diagram,

different behaviours could be observed between sandwich batches. Particularly, the impact depth data seem to highlight an almost inverse proportional trend as function of relative foam density of AFS-30 batch, whilst an almost flat decreasing trend is observed for AFS-20 samples. However, the correlation analysis between the foam density and the impact area evaluated on the binarized C-scan map could be observed in the Fig. 19 (b) for the two series of the tested specimens. In this diagram, the absence of a clear correlation between the impact sizes and relative foam density seems to be noted, as observed for the IRT data in previous section.

Specifically, the foam internal inhomogeneity due to non-uniform stochastic morphology and local density variability could affect the impact size data, while a more evident correlation is observed between the density of the foam and the impact depth. In fact, the measurement of average foam density is calculated for each AFS sample as indicated in equation (1). In literature, the X-ray tomographic technique is employed to define the morphological structure of foam core where the impact damage occurs, determining the local density in the impact areas for a proper correlative analysis as function of foam density [59–61].

IRT Processing Results

As shown in the Figs. 20 (a—b) and 21 (a—b), representative elaborated maps of TSR coefficients, EOF-1 and EOF-2 data are reported for AFS-20 P4 sample. In these processed maps, impact defective zone seems to appear as hot or cold spot area respect to the undamaged zone. Therefore, the binarization processing approach calculated as in equation (10) should be performed to process elaborated maps
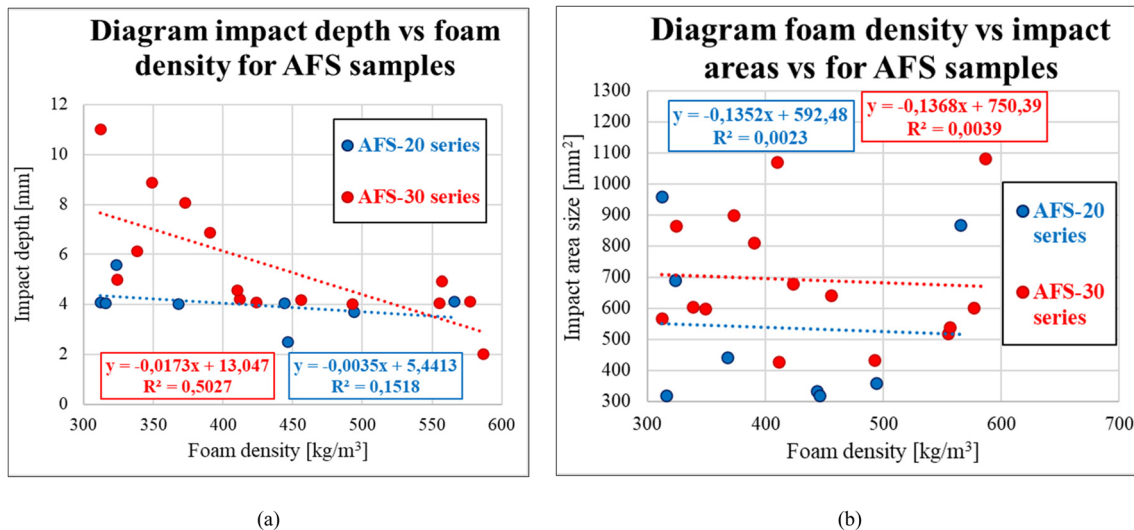

(a)   (b)

Fig. 19 (a) Impact depth data vs foam density and (b) impact area data evaluated on binarized maps vs foam density for AFS samples

as negative 2D matrix if impact damage appears as cold defective zone.

As described in the previous "Binarization for thermal data" section, the binarization processing methods evaluated

the single pixel of specific processed map, providing a value equal to one if its specific temperature satisfies the relationship of equation (11), otherwise the value is equal to zero. Then, the resulting binarized maps is processed providing
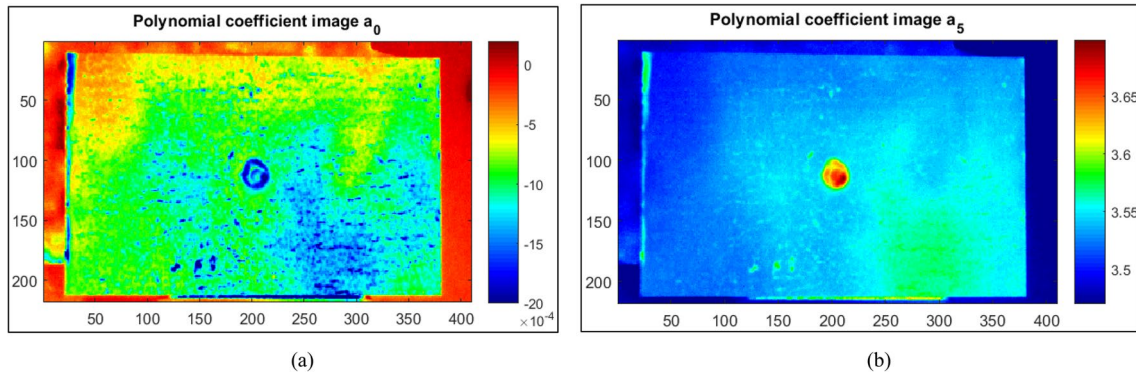

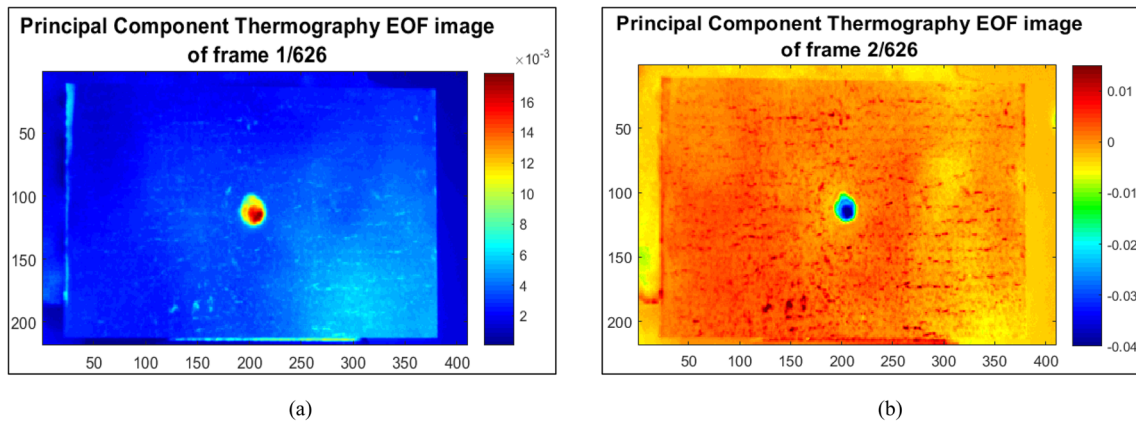**Fig. 20** (a) TSR coefficient a_0 and (b) a_5 maps for AFS-20 P4 panel

Fig. 21 (a) Principal component EOF-1 and (b) EOF-2 maps for AFS-20 P4 panel
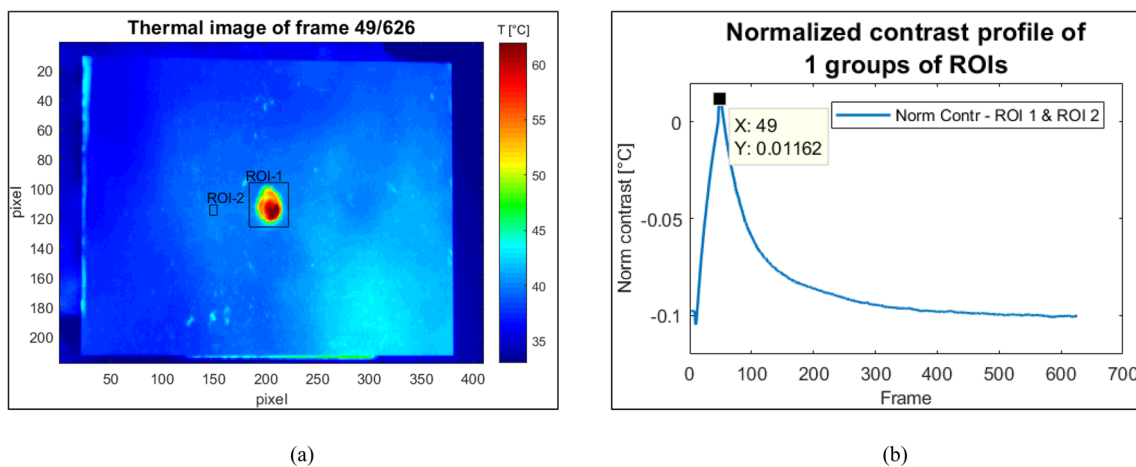

Fig. 22 (a) Raw thermal map with ROIs and (b) normalized contrast profile of couple of ROIs for AFS-20 P4 panel

a complete damage characterization in terms of size and shape, where the impact damage size is evaluated through the equation (10) in a quantitative manner. As anticipated in the paragraph 3.1, different processing approaches employed for PT are selected for impact damage quantification of AFS panels. Specifically, the binarization approach proposed for PT is performed on first and sixth TSR coefficients (using a polynomial fitting of fifth order), first and second EOF maps, statistical Skewness and Kurtosis maps and on the three LBC-II maps.

In addition, a specific raw thermal map is selected at the cooling time when the maximum value of normalized contrast of impacted zone occurs. For example, the representative raw image of AFS-20 P4 panel shown in Fig. 22 (a) is selected based on relative normalized contrast profile as function of acquired frames, as reported in Fig. 22 (b). This selection procedure represents a classical approach for defect sizing, based on the assumption that defect visibility is more performed at maximum contrast peak, when defect detection should be occurred [40]. However, the visibility of defects at maximum thermal contrast could be enhanced, but then the defect edge could be blurred for the 3D spreading of thermal front [40]. Thus, the predicted optimal detection

times of impacted damage involves almost $0.1 \div 0.5$ s after heating phase.

In previous Fig. 4 (a) and (b), the two representative images of impact damages seem to highlight the impact indentation on the laminated skin and the debonding of skin arisen after impactor indentation.

Therefore, a proper image—processing method should be performed for damage quantification, distinguishing also the different damaged zones. As shown in Fig. 23 (b) and (c), the two LBC – II processed maps seem to highlight different damage zones. Specifically, the boundary deformation zone is observed in the LBC-II approach A map (following equation (7)), whilst the impactor indentation area is noted in the map processed with LBC-II approach B (following equation (8)). However, the output map processed through LBC-II standard approach (following equation (6)) seems to include both damaged zones of simulated impact defect, as observed in Figs. 23 (a) and 24. In fact, the LBC-II standard method is based on the principle that computed temperatures around an inspected spot tend to reach similar values when location corresponds to defect border, leading to temporal contrast values being displayed with minimum values on contrast maps, clearly distinguishing the damage's edge [32].
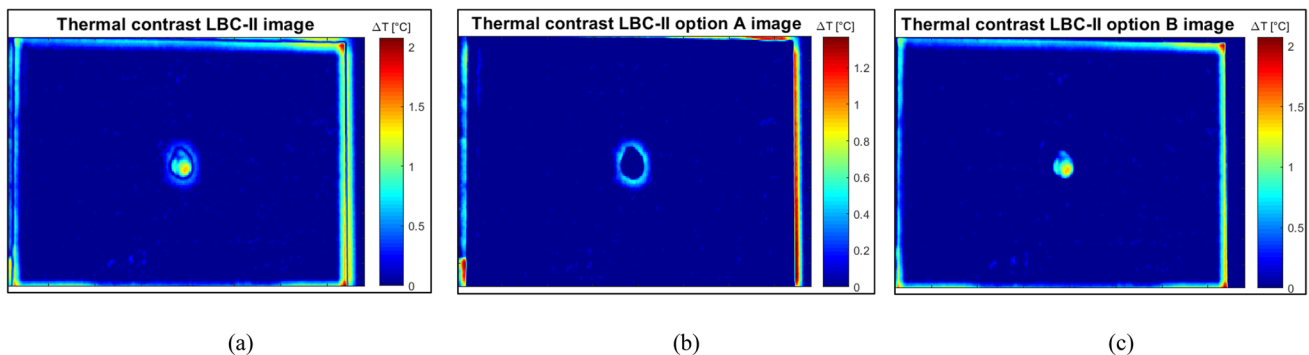

(a)　　　　　　　　(b)　　　　　　　　(c)

Fig. 23 (a) Processed map with LBC-II standard, LBC-II method A and (b) LBC-II method B for AFS-20 P4 panel
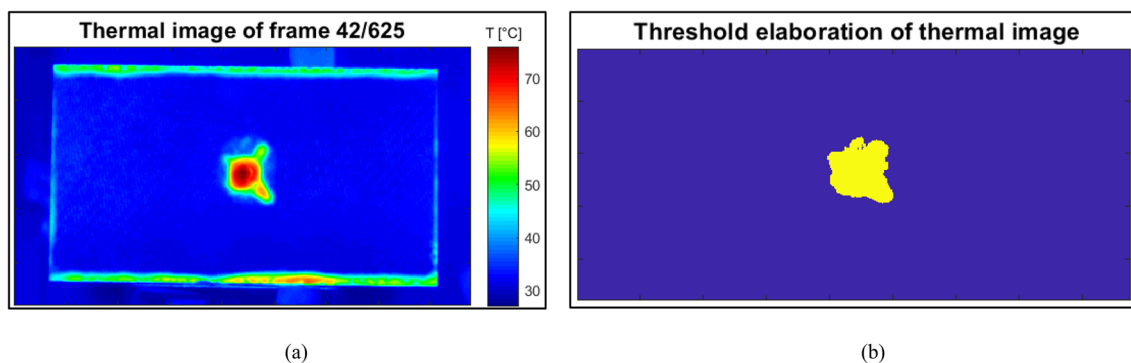

(a)　　　　　　　　(b)

Fig. 24 (a) Raw thermal and (b) relative binarized maps for AFS-20 P13 panel
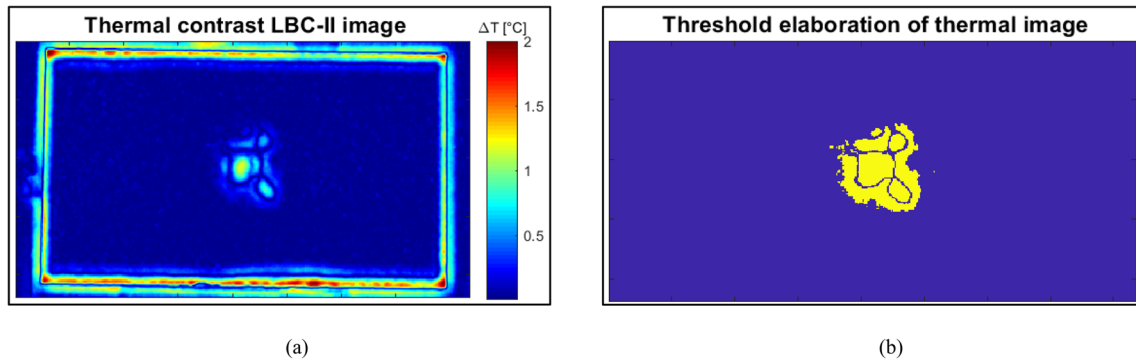
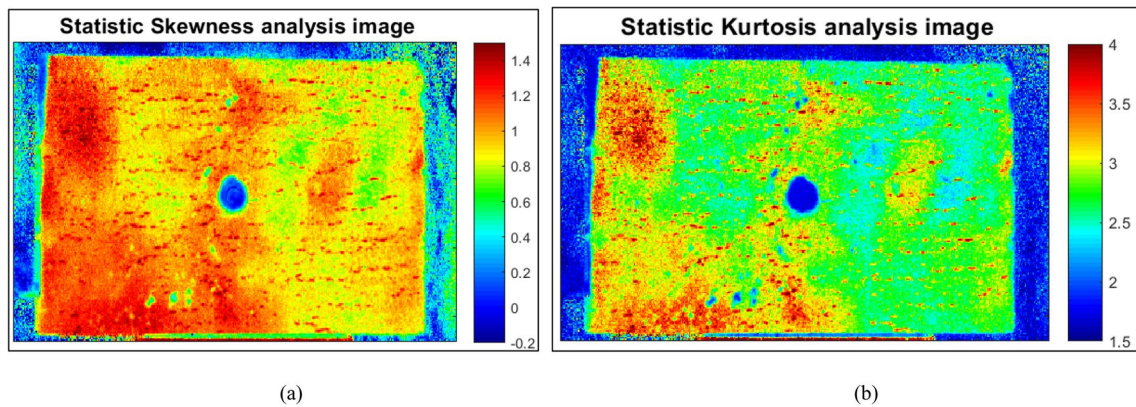**Fig. 25** (a) LBC-II standard and (b) relative binarized maps for AFS-20 P13 panel

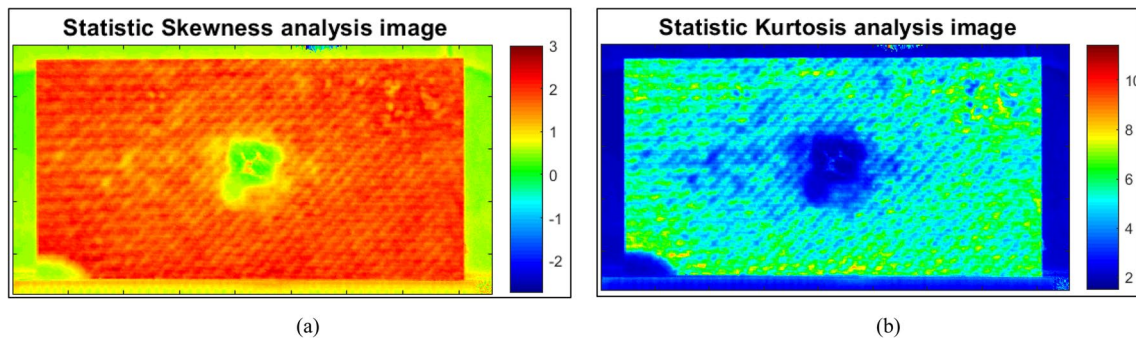**Fig.26** (a) Skewness and (b) kurtosis maps for AFS-20 P4 panel

Fig. 27 (a) Skewness and (b) kurtosis maps for AFS-30 P16 panel

Therefore, the LBC-II approach consists of an analogous binarized procedure, where the computation of impacted damage area could be clearly evaluated setting the threshold parameter T_{def_edge} equal to zero.

Therefore, the contrast-based maps processed through the standard LBC-II approach and the LBC-II approach B are selected for the binarization processing to evaluate the impact size of both AFS batches. As observed in

Figs. 23 (a) and 25 (a), the LBC-II standard maps seem to provide a boundary profile where the impacted damage indentation could be clearly distinguished by delamination zones. The same binarization of impact damage could be obtained combining the LBC-II approach A and the LBC-II approach B. However, the different damage zones appear merged in the other binarized maps, as observed in the example Fig. 24 (a) and (b), where the

raw thermal and relative binarized maps for AFS-20 P13 panel, respectively.

In Figs. 26 (a—b) and 27 (a—b), representative examples of processed thermal images through two statistical approaches based on standardization are reported. In the two maps of Fig. 26, the influence of lamination process and fibre orientation seem appear for the AFS-20 P4 sample more prominently than the previous TSR coefficient, EOF

and raw thermal maps. In addition, both statistical methods provide colder spot on the impacted areas for both AFS batches. Thus, the different binarization process is employed to convert the statistical images as a negative-values maps, providing higher values in damages zones.

However, the influence of stochastic morphology of Al foam and the laminated surface imperfections could affect the impacted zones in terms of shape, location, and size,
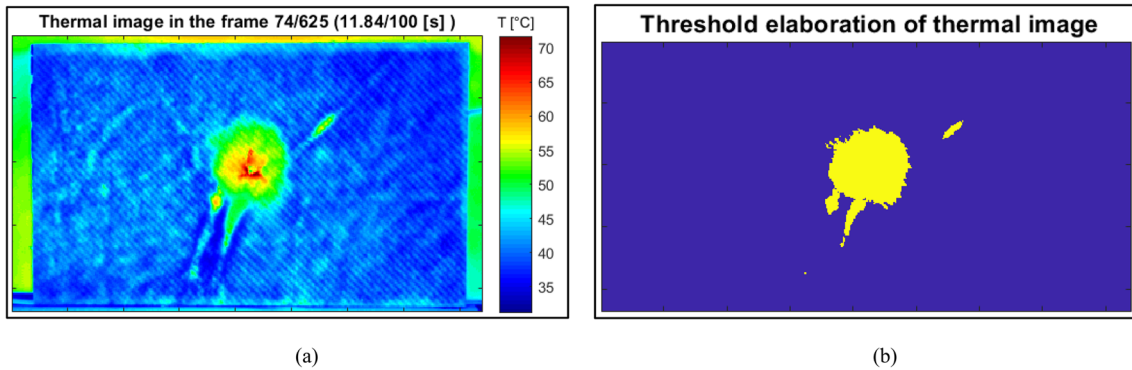

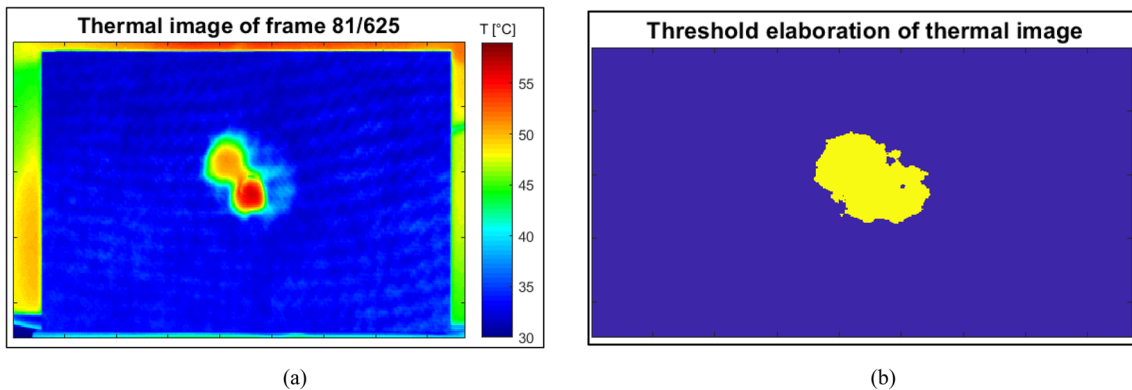**Fig. 28** (a) Raw thermal and (b) binarized maps of AFS-30 P23 panel

Fig. 29 (a) Thermal and (b) binarized maps of AFS-30 P28 panel
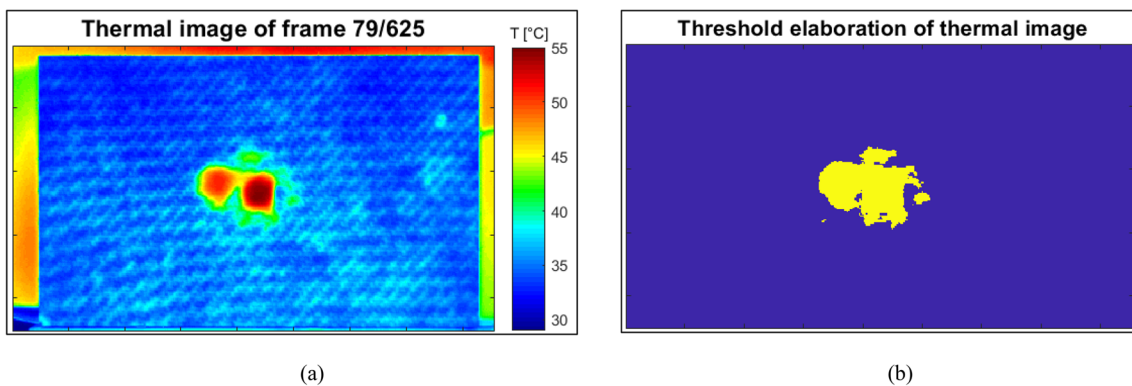

Fig. 30 (a) Thermal and (b) binarized maps of AFS-30 P33 panel

exhibiting different damage types under the same impact test conditions, as shown in Figs. 24 (a) and 27 (a) for the AFS-20 P13 and AFS-30 P16 samples, respectively. In addition, as reported in Fig. 28 (a), AFS-30 P23 panel seems more severely damaged than the other elements with diagonal wrinkles of 43.5 mm (bottom wrinkles) ÷ 23.05 (upper wrinkle) mm, confirming that IR techniques may be employed to detect damage lengths in components. Thus, the dark red region of impacted zone may also indicate severe damage modes such as foam crush and laminated skins crack.

In addition, damaged zones as double oval-shaped areas are observed at the centre of the impact point for AFS-30 P28 and AFS-30 P33 panels, as shown in Figs. 29 (a) and 30 (a). This impact defect shape could be due to local morphology with a widespread porosity in the Alulight foam that appears as a double-impact damage zone at the centre of panel. In addition, a discrete number of hot spots could be observed around this impact region, indicating delamination damage mode between skin sheet and Aluminium core. Therefore, this additional damaged zone is included in the binarized damaged area and appears as a merged yellow spot, as Figs. 29 (b) and 30 (b).

Table 6 Comparative analysis of impact damage sizing on AFS 20 sandwich panels

ID sample	Foam Density [kg/m³]	Impact area A_{IRT} [mm²]									Mean A_{IRT} [mm²]	Stand. Dev [mm²]
		Raw map	SKE map	KUR map	TSR Coeff a_0 map	TSR Coeff a_5 map	EOF-1 map	EOF-2 map	LBC-II std map	LBC-II B map		
AFS-20 P4	367.89	151.13	198.16	179.42	182.40	189.87	137.47	111.41	335.82	134.04	173.10	65.36
AFS-20 P5	311.85	628.47	668.70	786.37	767.14	775.64	555.27	389.18	905.01	531.88	676.13	158.96
AFS-20 P6	443.87	344.54	155.99	185.16	266.23	261.32	368.49	111.16	385.36	177.28	246.78	99.56
AFS-20 P11	315.67	282.61	219.14	259.82	230.60	221.15	246.36	233.18	298.83	179.93	241.53	35.76
AFS-20 P13	565.52	680.39	581.96	797.79	799.87	710.93	705.89	545.80	866.78	434.12	684.13	138.22
AFS-20 P15	323.37	631.97	521.01	818.46	538.04	684.43	645.43	603.13	686.32	694.79	641.63	89.81
AFS-20 P17	445.98	206.27	205.49	224.08	201.62	140.70	206.53	115.91	314.37	158.94	192.16	56.98
AFS-20 P19	493.84	308.302	204.304	263.12	194.93	151.74	258.576	129.57	303.19	133.83	216.13	69.90

Table 7 Comparative analysis of impact damage sizing on AFS 30 sandwich panels

ID Sample	Foam Density [kg/m³]	Impact area A_{IRT} [mm²]									Mean A_{IRT} [mm²]	Stand Dev [mm²]
		Raw map	SKE map	KUR map	TSR Coeff a_0 map	TSR Coeff a_5 map	EOF-1 map	EOF-2 map	LBC-II std map	LBC-II B map		
AFS-30 P4	576.81	310.46	396.75	402.29	319.75	332.70	333.00	299.78	543.22	257.35	349.38	83.81
AFS-30 P5	423.65	537.89	395.15	436.88	602.07	454.14	474.58	310.25	711.44	266.21	462.47	138.8
AFS-30 P6	555.06	403.85	271.06	405.37	389.87	297.50	393.83	265.589	653.34	335.78	365.20	117.2
AFS-30 P8	492.56	287.74	311.45	290.56	252.63	239.45	279.31	143.99	443.49	206.16	266.25	82.0
AFS-30 P10	411.66	628.45	531.40	619.86	507.22	601.09	526.94	361.76	503.46	345.82	536.37	102.5
AFS-30 P15	312.20	745.31	632.15	838.41	540.13	698.77	619.40	616.43	634.36	368.19	679.45	131.5
AFS-30 P16	324.17	721.20	705.35	955.06	433.09	806.85	571.37	619.43	1083.4	481.15	699.33	213.7
AFS-30 P19	338.13	679.70	717.82	997.12	628.61	504.91	613.31	583.75	701.68	391.07	682.71	166.9
AFS-30 P21	348.66	550.32	637.63	674.82	295.91	736.27	557.32	488.06	620.58	429.31	596.37	135.0
AFS-30 P23	372.88	1173.23	1087.95	1292.88	1094.15	609.10	1023.60	792.32	1001.2	856.40	1042.24	208.9
AFS-30 P24	390.58	981.60	1172.89	1052.47	870.68	580.79	867.34	768.49	1021.22	474.75	903.43	226.5
AFS-30 P27	410.09	1056.48	1211.08	1330.05	739.51	677.62	999.95	679.76	1314.78	457.64	947.58	314.8
AFS-30 P28	455.63	1135.50	1145.14	838.09	774.02	1282.6	851.11	693.54	667.56	439.62	959.20	270.3
AFS-30 P31	556.74	718.30	781.64	1238.36	722.16	915.51	723.97	442.82	630.56	291.70	773.11	269.0
AFS-30 P33	586.57	854.34	872.61	1053.24	903.68	498.30	865.31	611.06	1297.88	354.87	810.62	287.0

A specific conversion factor pixel / millimetre was estimated for each thermographic acquisition employing the well-known dimensions of the various samples. Then, the binarization processing approach is performed in each processed IR image to estimate the impact damage sizes, whose data results are reported Tables 6 and 7 for AFS 20 and AFS 30 panels, respectively. As observed in these Tables, several image-processing approaches seem to provide different estimation of impact sizes. Specifically, the statistical kurtosis, EOF—1 and TSR coefficient a_0 methods seem to over-estimate the damaged areas, whilst the statistical skewness, EOF—2 and TSR coefficient a_5 procedures show similar data variation with a percentage under the mean values. In addition, the higher values of impact sizes are observed in the data results of LBC-II standard approach, that includes the deformation areas in the sizing evaluation.

In particular, the double oval-shaped impacted damage size for AFS-30 P33 is equal as 1297.88 mm² evaluated through standard LBC-II method, resulting the greatest damage size among all the AFS panels, as reported in Table 7.

In addition, the impact size data obtained through different processing approaches are evaluated as function of foam density for AFS series. Therefore, a simpler definition of Signal to Noise Ratio is employed, evaluated as the ratio between the mean value (μ) and the standard deviation (σ) of the thermal measurements for each sample tested, including the influence of various data elaboration algorithms for both AFS-20 and AFS-30 reported in Tables 6 and 7 and calculated as [62]:

$$SNR = \frac{\mu}{\sigma} \tag{14}$$

Therefore, the signal to noise data of mean impact size A_{IRT} is assessed for each AFS element and correlated to specific foam density. As shown in Fig. 31 (a) and (b), the SNR data are reported as function of specific foam density of AFS-20 and AFS-30 elements, respectively.

In both diagrams, a general data variability seems to be clearly evident in each AFS batch, showing the results of best SNR values above to 6 for two AFS-20 panels, where the lower density and small porosity may avoid the boundary
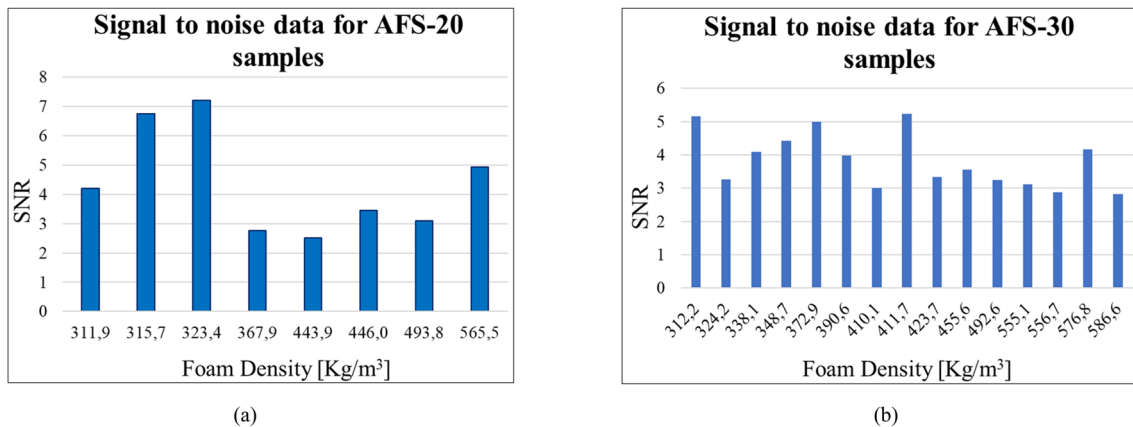

(a)

(b)

Fig. 31 (a) SNR data results vs foam density for AFS-20 and (b) AFS-30 elements

Table 8 Comparative analysis of impact damage sizing on AFS-20 sandwich panels

		[A_{IRT}—A_{UT}] / A_{UT} [%]								
		Raw map	SKE map	KUR map	TSR Coeff a_0 map	TSR Coeff a_5 map	EOF-1 map	EOF-2 map	LBC-II std map	LBC-II B map
ID Sample	AFS-20 P4	-65.77	-55.12	-59.37	-58.69	-57.00	-68.87	-74.77	-23.95	-69.64
	AFS-20 P5	-34.63	-30.45	-18.21	-20.21	-19.33	-42.25	-59.52	-5.87	-44.68
	AFS-20 P6	+3.06	-53.34	-44.61	-20.36	-21.83	+10.23	-66.75	+15.27	-46.97
	AFS-20 P11	-11.83	-31.63	-18.94	-28.06	-31.00	-23.14	-27.25	-6.77	-43.86
	AFS-20 P13	-21.75	-33.07	-8.25	-8.01	-18.24	-18.82	-37.23	-0.31	-50.07
	AFS-20 P15	-8.46	-24.53	+18.56	-22.06	-0.86	-6.51	-12.63	-0.58	+0.64
	AFS-20 P17	-35.71	-35.95	-30.16	-37.16	-56.15	-35.63	-63.87	-2.02	-50.46
	AFS-20 P19	-14.27	-43.19	-26.84	-45.80	-57.81	-28.10	-63.97	-15.70	-62.79

Table 9 Comparative analysis of impact damage sizing on AFS-30 sandwich panels

		[A_{IRT}—A_{UT}] / A_{UT} [%]								
		Raw map	SKE map	KUR map	TSR Coeff a_0 map	TSR Coeff a_5 map	EOF-1 map	EOF-2 map	LBC-II std map	LBC-II B map
ID Sample	AFS-30 P4	-48.47	-34.14	-33.22	-46.92	-44.77	-44.72	-50.24	-9.83	-57.28
	AFS-30 P5	-20.96	-41.94	-35.80	-11.53	-33.27	-30.27	-54.41	+4.54	-60.88
	AFS-30 P6	-22.52	-48.00	-22.23	-25.20	-42.93	-24.45	-49.05	+25.34	-35.58
	AFS-30 P8	-33.81	-28.36	-33.17	-41.89	-44.92	-35.75	-66.88	+2.01	-52.58
	AFS-30 P10	+46.55	+23.92	+44.55	+18.28	+40.17	+22.88	-15.64	+17.40	-19.36
	AFS-30 P15	+31.23	+11.30	+47.62	-4.90	+23.03	+9.06	+8.54	+11.69	-35.17
	AFS-30 P16	-16.70	-18.53	+10.31	-49.98	-6.81	-34.01	-28.46	+25.13	-44.43
	AFS-30 P19	+12.29	+18.59	+64.73	+3.85	-16.59	+1.32	-3.56	+15.92	-35.39
	AFS-30 P21	-8.41	+6.12	+12.31	-50.75	+22.53	-7.25	-18.78	+3.28	-28.55
	AFS-30 P23	+30.17	+20.71	+43.44	+21.39	-32.42	+13.57	-12.09	+11.08	-4.98
	AFS-30 P24	+20.86	+44.42	+29.59	+7.21	-28.49	+6.80	-5.38	+25.74	-41.54
	AFS-30 P27	-1.47	+12.95	+24.04	-31.03	-36.80	-6.74	-36.60	+22.62	-57.32
	AFS-30 P28	+157.03	+159.21	+89.71	+75.20	+190.33	+92.65	+56.99	+4.02	-0.49
	AFS-30 P31	+33.06	+44.79	+129.40	+33.78	+69.59	+34.11	-17.97	+16.81	-45.96
	AFS-30 P33	-21.19	-19.50	-2.84	-16.63	-54.03	-20.17	-43.63	+19.73	-67.26

problem evaluation around damages areas. However, the experimental results provide lower SNR values under 4 for several defective areas that represent an unsatisfactory evaluation for the requirements of accurate detection and characterization of interface impacted damage of sandwich structures.

Comparative Analysis Between UT and IRT Data

In this paragraph, a comparative analysis is performed between IRT and UT results for the impact size quantification on the two AFS series. Particularly, the obtained values of impacted areas evaluated on binarized IRT maps (denoted as A_{IRT} [mm^2]) are compared with the reference resulting areas calculated from binarized C-scan maps (indicated as A_{UT} [mm^2]). Data results of comparative analysis are reported in Tables 8 and 9 for AFS-20 and AFS-30 elements, respectively. In both impacted series, an evident data variation respect to ultrasonic measurements is observed in terms of impact area sizes between the different employed processing approaches. Both positive and negative percentage variations are observed in each IRT processed map respect to the relative UT data. However, the data results seem to indicate an evident underestimation of the impact damage sizes evaluated with IRT processing methods related to the UT data. In the AFS-20 series, a general behaviour with a negative percentage variation is observed respect to AFS-30 elements.

Moreover, a greater percentage variation is observed in AFS-30 P28 sample, where the previous IRT maps highlight the presence of a "double" impacted area as shown in Fig. 29 (a), whilst a different impact area is observed in the corresponding C-scan maps, as reported in the example of Fig. 17 (a). This phenomenon, in the opinion of the authors, could be motivated by the morphological structure of the foam and by the possible presence of a widespread porosity in the neighbouring region to the impacted areas.

The impact sizing results obtained through the binarized LBC-II standard maps seem to provide proper damage area quantification compared to UT data in both series of the specimens with the lowest percentage variations. In particular, the maximum data deviations around 25% was observed for three AFS-30 samples (in particular P6, P16 and P24 elements). The LBC-II method B results seem to clearly underestimate the impact area respect to the LBC-II standard data, because only the damage zone of impact indentation area is evaluated in the sizing quantification, without delaminated and deformed damage zones in the impact area estimation.

Conclusions

In the present work, different Non-Destructive processing approaches for pulsed thermographic method are performed for impact size quantification on two series of AFS laminated sandwich panels, indicated as AFS-20 and AFS-30 elements. Specifically, the well-stablished processing methods (TSR, PCT Skewness and Kurtosis,) and three

proposed contrast-based procedures (denoted as LBC-II approaches) are employed and compared with the reference data obtained through ultrasonic PA inspections. Specific custom binarization procedures are implemented in MATLAB codes to process the IRT images or ultrasonic C-scan maps, assigning a threshold value selected based on the average values of the undamaged zones evaluated in specific regions of interest.

Concerning the selected processing approaches, the proposed LBC-II algorithm provides a single processed contrast map that seems to enhance both the accuracy of defect inspection and also the identification of damage boundaries according to spatial variations in neighbouring area of defective zone.

Specifically, the three proposed LBC-II elaboration approaches seem to provide output contrast maps that highlight the deformed boundary areas (with LBC-II method A), the central impactor indentation zone (with LBC-II method B) or both damaged zones (with LBC-II standard method) in processed images.

A greater percentage variation of impact sizes data is observed in both AFS series, due to the morphological structure of the foam and by the possible presence of a widespread porosity in the neighbouring region to the impacted areas. However, the comparative analysis between LBC-II standard maps and C-scan maps provide optimal data results in terms of damaged area quantification and qualitative damage inspection, highlighting also the area of detachment of the skin around impact zone.

Therefore, this case of study seems to confirm the importance of research efforts to perform advanced elaboration algorithms to improve defect detection and damage sizing quantification in terms of time-computation and accuracy for different industrial materials.

Declarations

Conflict of Interest The authors declare no conflict of interest.

References

1. Ruixiang B, Jingjing G, Zhenkun L, Da L, Yu M, Cheng Y (2019) Compression after impact behavior of composite foam-core sandwich panels. Compos Struct 225:111181. https://doi.org/10.1016/j.compstruct.2019.111181
2. Vinson JR (2001) Sandwich structures. Appl Mech Rev 54(3):201–214. https://doi.org/10.1115/1.3097295
3. Baumeister J, Banhart J, Weber M (1997) Aluminum foams for transport industry. Mater Des 18(4):217–220
4. Altenbach H (2011) Mechanics of advanced materials for lightweight structures. Proc Inst Mech Eng C J Mech Eng Sci 225(11):2481–2496
5. Srinath G, Vadiraj A, Balachandran G, Sahu SN, Gokhale AA (2010) Characteristics of aluminium metal foam for automotive applications. Trans Indian Inst Met 63(5):765–772
6. Crupi V, Epasto G, Guglielmino E (2016) Internal damage investigation of composites subjected to low-velocity impact. Exp Tech 40:555–568. https://doi.org/10.1007/s40799-016-0057-1
7. Singh S, Bhatnagar N (2018) A survey of fabrication and application of metallic foams (1925–2017). J Porous Mater 25(1). https://doi.org/10.1007/s10934-017-0467-1
8. Banhart J, Schmoll C, Neumann U (1998) Light-weight aluminium foam structures for ships. Proceedings of Conference Materials in Oceanic Environment (Euro-mat '98), Lisbon, Portugal, July 22–24 1998, vol. 1, 55 – 63
9. Cho U, Hong SJ, Lee SK, Cho C (2012) Impact fracture behaviour at the material of aluminium foam. Mater Sci Eng A 539:250–258
10. Abrate S (1998) Impact on Composite Structures. Cambridge University Press, Cambridge (ISBN 9780521473897)
11. Sutherland LS (2018) A review of impact testing on marine composite materials: part I—Marine impacts on marine composites. Compos Struct 188:197–208
12. Akil Hazizan M, Cantwell WJ (2003) The low velocity impact response of an aluminium honeycomb sandwich structure. Compos Part B Eng 34:679–687
13. Mohd FI, Aidah J, Nurulnatisya A, Muhammad HI (2015) Low velocity impact of aluminium foam -glass fibre reinforced plastic sandwich panels. Adv Mater Res 1113:74–79
14. Ahmed S, Lee S, Cho C, Choi KK (2011) Experimental study on low velocity impact response of CFRP - aluminum foam core sandwich plates, 18th International Conference on Composite Materials. Jeju, Korea, in Proc. of ICCM18
15. Villanueva GR, Cantwell WJ (2003) Low velocity impact response of novel fiber-reinforced aluminum foam sandwich structures. J Mater Sci Lett 22:417–422
16. Xie Honglei, Fang Hai, Li Xiaolong, Wan Li, Peng Wu, Yi Yu (2021) Low-velocity impact damage detection and characterization in composite sandwich panels using infrared thermography. Compos Struct 269:114008. https://doi.org/10.1016/j.compstruct.2021.114008
17. Saharudin MS, Jumahat A, Kahar AZA, Ahmad S (2013) The influence of alumina filler on impact properties of short glass fiber reinforced epoxy. Appl Mech Mater 393:88–93. https://doi.org/10.4028/www.scientific.net/amm.393.88
18. Hayman B (2007) Approaches to damage assessment and damage tolerance for FRP sandwich structures. J Sandwich Struct Mater 9(6). https://doi.org/10.1177/1099636207070853
19. Nsengiyumva W, Zhong S, Lin J, Zhang Q, Zhong J, Huang Y (2021) Advances, limitations and prospects of non-destructive testing and evaluation of thick composites and sandwich structures: a state-of-the-art review. Compos Struct 256:112951. https://doi.org/10.1016/j.compstruct.2020.112951

20. Růžek R, Lohonka R, Jironč J (2006) Ultrasonic C-Scan and shearography NDI techniques evaluation of impact defects identification. NDT E Int 39(2):132–142. https://doi.org/10.1016/j.ndteint.2005.07.012

21. Khan MH, Elamin M, Li B, Tan KT (2018) X-ray micro-computed tomography analysis of impact damage morphology in composite sandwich structures due to cold temperature arctic condition. J Compos Mater 52(25). https://doi.org/10.1177/0021998318785671

22. Vavilov VP, Nesteruk DA (2004) Detecting water in aviation honeycomb structures: the quantitative approach. Quant Infra-Red Thermogr J 1(2):173–184. https://doi.org/10.3166/qirt.1.173-184

23. Drinkwater BW, Wilcox PD (2006) Ultrasonic arrays for non-destructive evaluation: a review. NDT E Int 39(7):525–541. https://doi.org/10.1016/j.ndteint.2006.03.006

24. Schaal C, Mal A (2017) Core-skin disbond detection in a composite sandwich panel using guided ultrasonic waves. J Nondestruct Eval Diagnostics Progn Eng Syst 1(1):011006

25. Taheri H, Hassen AA (2019) Non-destructive ultrasonic inspection of composite materials: a comparative advantage of phased array ultrasonic. Appl Sci 9:1628

26. Katunin A, Dragan K, Dziendzikowski, (2015) Damage identification in aircraft composite structures: a case study using various non-destructive testing techniques. Compos Struct 127:1–9. https://doi.org/10.1016/j.compstruct.2015.02.080

27. Katunin A, Katunin MC-K (2015) Assessment of internal damages in sandwich panels via active thermography. Eng Trans 63(2):171–180

28. Ibarra-Castanedo C, Piau JM, Guilbert S, Avdelidis NP, Genest M, Bendada A, Maldague XP (2009) Comparative study of active thermography techniques for the nondestructive evaluation of honeycomb structures. Res Nondestr Eval 20(1):1–31

29. Ciampa F, Mahmoodi P, Pinto F, Meo M (2018) Recent advances in active infrared thermography for non-destructive testing of aerospace components. Sensors 18:609. https://doi.org/10.3390/s1802060

30. Nobile R, Panella FW, Pirinu A, Saponaro A (2021) Bending residual strength of damaged Al foam sandwiches through UT and IRT analyses. Proc Struct Integ 33(8):685–694. https://doi.org/10.1016/j.prostr.2021.10.076

31. Jones RM (1999) Mechanics of Composite Materials. Taylor & Francis, Inc., Chapter 2: Macro mechanical Behaviour of a lamina

32. Panella FW, Pirinu A (2021) Application of pulsed thermography and post-processing techniques for cfrp industrial components. J Non-destructive Eval 40(2). https://doi.org/10.1007/s10921-021-00776-8

33. Panella FW, Pirinu A, Dattoma V (2020) A brief review and advances of thermographic image - processing methods for IRT inspection: a case of study on GFRP plate. Exp Tech 45(2). https://doi.org/10.1007/s40799-020-00414-4

34. Dattoma V, Nobile R, Panella FW, Pirinu A, Saponaro A (2018) Optimization and comparison of ultrasonic techniques for NDT control of composite material elements. Procedia Struct Integrity 12:9–18. https://doi.org/10.1016/j.prostr.2018.11.111

35. Dattoma V, Panella FW, Pirinu A, Saponaro A (2019) Advanced NDT methods and data processing on industrial CFRP components. Appl Sci 9(3):393. https://doi.org/10.3390/app9030393

36. Ciampa F, Mahmoodi P, Pinto F, Meo M (2018) Recent advances in active infrared thermography for non-destructive testing of aerospace components. Sensors 18(2):609. https://doi.org/10.3390/s18020609

37. Chung Y, Lee S, Kim W (2021) Latest advances in common signal processing of pulsed thermography for enhanced detectability: a review. Appl Sci 11(24):12168. https://doi.org/10.3390/app112412168

38. Vavilov V, Chulkov AO, Shiryaev VV (2022) Practical limits of pulsed thermal NDT: the concept of additive/ multiplicative noise. NDT E Int 130(1):102677. https://doi.org/10.1016/j.ndteint.2022.102677

39. Ibarra-Castanedo C, Tarpani JR, Maldague XPV (2013) Non-destructive testing with thermography. Eur J Phys 34(6):S91–S109. https://doi.org/10.1088/0143-0807/34/6/S91

40. Ibarra-Castanedo C, Maldague X (2013) Handbook of Technical Diagnostics: Fundamentals and Application to Structures and Systems, Part II: Methods and Techniques for Diagnostics and Monitoring, Cap. 10: Infrared Thermography, Horst Czichos Editor, Springer Science & Business Media, ISBN - 9783642258503

41. Theodorakeas P, Avdelidis NP, Ibarra-Castanedo C, Koui M, Maldague X (2014) Pulsed thermographic inspection of CFRP structures: experimental results and image analysis tools. Proceedings of SPIE. https://doi.org/10.1117/12.2044687

42. Khodayar F, Sojasi S, Maldague X (2015) Infrared Thermography and NDT: 2050 Horizon. In Proc. QIRT 2015. https://doi.org/10.21611/qirt.2015.0001

43. Ibarra-Castanedo C, Genest M, Piau JM, Guibert S, Bendada A, Maldague XPV (2007) Active infrared thermography NDT techniques, ultrasonic and advanced methods for nondestructive testing and material characterization, pages 325–348. https://doi.org/10.1142/9789812770943001 4

44. Shepard SM, Lhota JR, Rubadeux BA, Wang D, Ahmed T (2003) Reconstruction and enhancement of active thermographic image sequences. Opt Eng 42(5). https://doi.org/10.1117/1.1566969

45. Shepard SM, Lhota JR, Rubadeux BA, Ahmed T, Wang D (2002) Enhancement and reconstruction of thermographic NDT data. Proc. Thermosense XXIV - Aero-Sense. https://doi.org/10.1117/12.459603

46. Shepard SM, Hou J, Lhota JR, Golden JM (2007) Automated processing of thermographic derivatives for quality assurance. Opt Eng. https://doi.org/10.1117/1.2741274

47. Zheng K, Chang YS, Wang KH, Yao Y (2015) Improved non-destructive testing of carbon fiber reinforced polymer (CFRP) composites using pulsed thermography. Polym Test. https://doi.org/10.1016/j.polymertesting.2015.06.01644

48. Balageas D, Roche JM (2014) Common tools for quantitative time-resolved pulse and step-heating thermography – part I: theoretical basis. Quant InfraRed Thermogr J. https://doi.org/10.1080/17686733.2014.891324

49. Balageas D, Roche J-M, Leroy F-H (2013) Les images de coefficients de la méthode TSR (Thermographic Signal Reconstruction): un moyen simple et efficace de détecter et imager les défauts; Annual Conf. Société Française de Thermique, Gérardmer (France) 28–31 May 2013

50. Roche J-M, Leroy F-H, Balageas D (2014) Images of TSR coefficients: a simple way for a rapid and efficient detection of defects. Mater Eval 72(1):73–82

51. Rajic N (2002) Principal component thermography, defense science and technology organization victoria (Australia) aeronautical and maritime research laboratory, technical report DSTO-TR-1298. Available online: https://apps.dtic.mil/dtic/tr/fulltext/u2/a405857.pdf. Accessed Dec 2022

52. Rajic N (2000) A quantitative approach to active thermographic inspection for material loss evaluation in metallic structures. Res Nondestr Eval 12(2):119–131. https://doi.org/10.1007/s001640000008

53. Wall ME, Rechtsteiner A, Rocha LM (2003) Singular value decomposition and principal component analysis. In: Berrar DP, Dubitzky W, Granzow M (eds) A Practical Approach to Microarray Data Analysis. Kluwer, Norwell, pages 91–109. LANL LA-UR-02–4001

54. Madruga FJ, Ibarra-Castanedo C, Condea OM et al (2010) Infrared thermography processing based on higher-order statistics. NDT E Inter 43(8):661–666

55. Madruga FJ, Ibarra-Castanedo C, Conde OM, Maldague XP, López-Higuera JM (2009) Enhanced contrast detection of subsurface defects by pulsed infrared thermography based on the fourth order statistic moment, kurtosis. Proceedings of SPIE 7299: 72990U (8 pp.). https://doi.org/10.1117/12.818684

56. Madruga FJ, Ibarra-Castanedo C, Conde OM, Lopez-Higuera JM, Madalgue X (2008) Automatic data processing based on the skewness statistic parameter for subsurface defect detection by active infrared thermography. In: Proc. of he ninth international conference QIRT

57. Hidalgo-Gato R, Andrés JR, López-Higuera JM, Madruga FJ (2013) Quantification by signal to noise ratio of active infrared thermography data processing techniques. Opt Photon J. https://doi.org/10.4236/opj.2013.34A0043

58. Sfarra S, Theodorakeas P, Ibarra-Castanedo C, Avdelidis NP, Ambrosini D et al (2015) How to retrieve information inherent to old restorations made on frescoes of particular artistic value using infrared vision? Int J Thermophys. https://doi.org/10.1007/s10765-015-1962-859

59. De Giorgi M, Carofalo A, Dattoma V, Nobile R, Palano F (2010) Aluminium foams structural modelling. Comput Struct 88(1–2):25–35. https://doi.org/10.1016/j.compstruc.2009.06.005

60. Maire E, Fazekas A, Salvo L, Dendievel R, Youssef S, Cloetens P et al (2003) X-ray tomography applied to the characterization of cellular materials. Related finite element modeling problems. Compos Sci Technol 63:2431–2443

61. Crupi V, Epasto G, Guglielmino E (2013) Computed Tomography analysis of damage in composite subjected to impact loading. Frattura Integrità Strutturale 5(17). https://doi.org/10.3221/IGF-ESIS.17.04

62. González RC, Woods RE (2008) Digital image processing. Prentice Hall. p. 354. ISBN 978–0–13–168728–8